Evaporation-induced non-wetting droplets on superhydrophilic surfaces

by
Solomon Adera
BSME Georgia Institute of Technology

Submitted to the Department of Mechanical Engineering in
Partial Fulfillment of the Requirements for the
Degree of Master of Science in Mechanical Engineering
at the
Massachusetts Institute of Technology
September 2012

Signature of Author:.....
Department of Mechanical Engineering
August 20, 2012

Certified by:.....
Evelyn N. Wang
Associate Professor of Mechanical Engineering
Thesis Supervisor

Accepted by:.....
David E. Hardt
Chairman, Department Committee on Graduate Thesis

Evaporation-induced non-wetting droplets on superhydrophilic surfaces

by
Solomon Adera

Submitted to the Department of Mechanical Engineering in August 20, 2012, in Partial Fulfillment of the Requirements for the Degree of Master of Science

Abstract

A droplet deposited on a rough, lyophilic surface satisfying the imbibition condition, results in spontaneous spreading and hence complete wetting. However, in this thesis, we demonstrate that this wetting behavior can be altered by superheating the substrate such that droplets can reside in a non-wetting state due to evaporation.

Photolithography and deep reactive ion etching were used to fabricate well-defined silicon micropillar arrays with a square pattern with varying pillar diameter, height, and center-to-center spacing. Water droplets placed on these microstructured surfaces at room temperature demonstrated superhydrophilic behavior with liquid filling the voids between pillars resulting in very low contact angle, and hence complete wetting. However, when the microstructured surface was superheated above a critical superheat, the superhydrophilicity was lost and non-wetting droplets were formed on the top surface of the micropillar array structure. The superheat required to deposit a non-wetting droplet ($> 75^{\circ}C$) was found to be significantly higher than that required to sustain an already deposited non-wetting droplet ($< 35^{\circ}C$). Moreover, the superheat required to sustain a non-wetting droplet after the initial deposition was observed to decrease with the square of the droplet radius. A 1-D lubrication type model based on a force balance between the wetting and non-wetting forces is developed which explains the mechanism by which non-wetting droplets can reside on superhydrophilic surfaces at superheated conditions due to induced evaporation. Moreover, the model predicts a square relationship between the superheat required to form non-wetting droplets and the droplet radius which is in agreement with experimental observation. These observations where non-wetting droplets reside on superhydrophilic surfaces at superheated conditions have implications for phase-change based heat transfer applications where the loss of contact between the substrate and the heat transfer fluid could be detrimental to the device performance.

Thesis Supervisor: Evelyn N. Wang
Title: Associate Professor, Mechanical Engineering

Acknowledgements

Above all, I praise the Lord, the almighty God for the wisdom and perseverance that He has bestowed upon me. I would not have made it this far without His blessing in my work and in my life. He is my protector, my strength, my deliverer, my stronghold, and my savior.

This thesis appears in the current form due to the assistance and guidance of several people that I am fortunate enough to come across in my life. Therefore, I would like to offer my sincere thanks to the following people.

First and foremost, I must express my deepest appreciation for the enthusiastic and dedicated guidance of my advisor, Professor Evelyn Wang. I would have been lost without her selfless support and guidance in my development as a researcher. I am extremely grateful for her unwavering help, encouragement and invaluable advice.

Next, I thank Dr. Rishi Raj for his follow up on my work. His challenge and critique helped me to improve my work in more ways than one. His counseling on my ever-improving technical writing skills was helpful. I am thankful for his availability for discussion in addition to reviewing this thesis.

I would like to thank Dr. Ryan Enright and all my fellow lab mates including postdocs for assistance.

I would also like to thank the staffs at the Microsystems Technology Laboratory (MTL), Center for Material Science and Engineering (CMSE) and Central Machine Shop at the Massachusetts Institute of Technology for technical assistance.

Finally, I want to thank my family for supporting me. I would not be where I am today without your unwavering help and encouragement. I cannot thank you enough for everything you have done in my life. God bless you all.

Contents

List of Figures

CHAPTER 1

1. Introduction

Thermal management is a critical limitation for a variety of high power density applications such as integrated circuits (ICs), microprocessors, and energy conversion devices. The performance and reliability of these devices is limited by the rate at which thermal energy can be removed from the foot print which is well above 100 W/cm^2 in most cases. Traditional cooling schemes such as forced convection cannot address such enormous cooling requirements. Hence, novel thermal management solutions are required to efficiently remove high thermal loads from these power-dense systems. In the first section of this chapter, we will present the thermal management challenges and the different cooling schemes currently is use to meet the demand from the industry for high heat load removal. Section 1.2 discusses the effect of roughness on phase-change heat transfer processes. The motivation for this thesis and its objective is discussed briefly in the last two sections.

1.1 Thermal Management Challenges

Extremely localized high heat fluxes are encountered in numerous high-energy devices. In the 1990's, for example, the heat flux of the original Pentium central processing unit was around 30 W/cm^2 and cooling was achieved through forced convection. However, due to increased transistor density, processing speed and miniaturization, the total heat generation and the heat flux at the electronics foot print has now increased to 200-1500 W/cm^2 [1]. Such high heat fluxes cannot be removed by traditional methods of forced air convection.

Fusion reactors, another example, contain components that require continuous cooling on the order of 10^4 W/cm^2 [2]. Other examples include direct energy devices such as synchrotron sources that deliver high energy x-ray beams with unprecedented power densities as high as $1.5x10^4$ W/cm^2 [3]. To effectively reject the high heat load, liquid cooling and phase-change heat transfer which utilize the great potential imbedded in the latent heat of vaporization of the coolant have been considered. Phase-change heat transfer is marked by relatively very high heat flux removal with low superheat. The effectiveness of the major cooling techniques is presented by Mudawar [4] and the comparison is shown in Fig. 1-1.

There are different kinds of phase-change cooling techniques such as pool boiling, flow boiling, jet impingement and spray cooling [4, 5]. Generally speaking, cooling techniques that employ phase-change are more difficult to implement but they are more efficient than their counterpart that utilize only sensible heat to remove waste heat. The advantages and challenges of the most widely used phase-change heat transfer techniques will be discussed briefly.

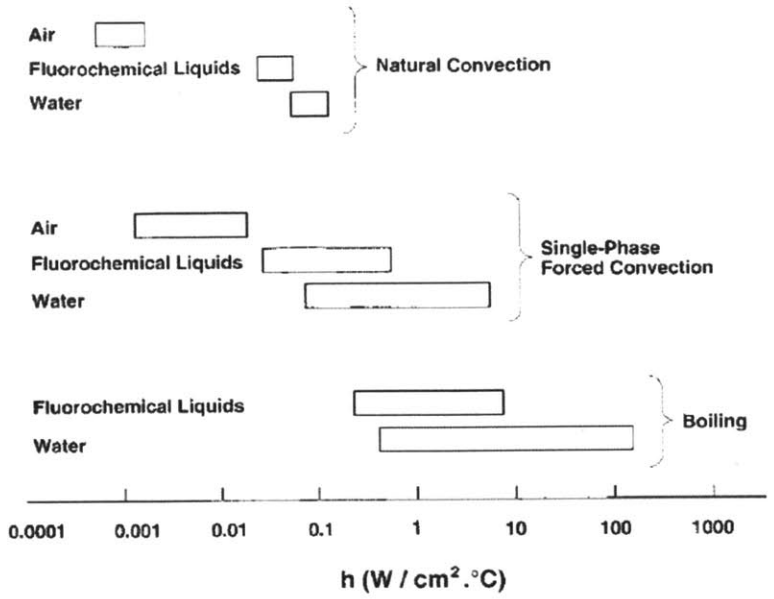

Figure 1-1: Comparison of attainable heat transfer coefficients of various cooling techniques using various coolants [4].

Pool boiling, which has been studied extensively in the past [6-9], is the simplest method of cooling heated surfaces that utilizes phase-change. The maximum heat flux and the cooling capacity, however, are limited by the critical heat flux (CHF), above which the transition from nucleate boiling to film boiling occurs. Film boiling is characterized by a significant increase in thermal resistance because of the low thermal conductivity of vapor which separates the liquid from being in contact with the heated surface, and hence very poor heat transfer mechanism. The CHF for water at ambient pressure on a flat surface has been shown to be roughly 110 W/cm^2 [10]. Extensive work has focused on enhancing the CHF limits on pool boiling. Such efforts include adding nanoparticles in the coolant and using textured surfaces to enhance surface wettability and increase surface area of contact between the heated surface and the coolant. You *et al.* [11] reported a 200% increase in CHF by using nanofluids that contain 0.005 g/L of alumina nanoparticles. Chu *et al.* [12] experimentally demonstrated a 200% increase in the CHF by using structured surfaces. They attributed the enhancement to increase in surface roughness and the associated roughness-amplified capillary forces. Kim *et al.* [9] on the other hand suggested that a 400% enhancement in CHF is possible by reducing the contact angle from 70° to 20°. Lastly, Chen *et al.* [13] used nanowires and nanotubes to enhance heat transfer and improve CHF. Microstructuring enhances heat transfer and improves CHF by introducing surface roughness that increases surface wettability and liquid spreading by generating a capillary pressure which assists liquid spreading. Moreover, the cavities within the microstructure act as additional nucleation sites for bubble growth that ultimately increase the active nucleation site density.

Flow boiling has shown promising results for removing high heat flux. Due to the high surface area to volume ratio, flow boiling in microchannels can be more efficient than its macroscale counterpart. At these small length scales, surface forces dominate over body forces.

However, due to the large viscous loss that is associated with the smaller length scale, this method suffers from significant pressure losses which can be as high as 1 atm in microchannels. This necessitates the need for high pumping power that ultimately limits its practical applicability in devices. Another problem with microchannel flow boiling is that bubbles tend to remain in the channel and grow longitudinally which will constrict the flow and may potentially cause flow reversal [4]. This flow constriction causes hot spots and flow instabilities which are characteristic features of microchannel flow.

In jet impingement cooling scheme, high speed jets from nozzles impinge on the heated surface and form a very thin layer of cooling fluid. The cooling effect is directly affected by the jet velocity and the sub-cooling of the impinging liquid. Wang *et al.* [14] used multiple microjet array of diameters 40-76 μm to cool VLSI (very large-scale integration) chips with wall temperature rise of 100 °C demonstrating a potential technology for integrated circuit (IC) chip cooling. Generally speaking, jet impingement is difficult to implement and it's characterized by non-uniformity in cooling where only the local jet impinged area experiences significant cooling and the remaining area experiences over flooding of coolant. The non-uniformity in cooling limits its implementation for practical use.

Similar to jet impingement, multiphase spray cooling uses liquid droplets to impinge on heated surfaces. The impingement creates a thin layer of liquid with significant contact line length that spreads and evaporates from the heated surface. Lin *et al.* [15] reported a 500 W/cm^2 heat flux by employing eight nozzles that used water as the cooling fluid. However, creating sprays requires a significant pressure that potentially consumes power and this makes spray cooling unattractive for commercial applications. Another concern that limits the use of spray cooling is the intricate flow pattern of the cooling fluid.

Recently, growing interest has focused on structured surfaces to enhance heat removal and meet the ever-increasing demand of the industry for higher heat load removal [9, 11, 12, 16]. Studies have demonstrated that roughness assists liquid spreading and enhance contact between the heated surface and coolant which ultimately increases the rate of heat transfer. The high surface tension forces offered by liquids in copper and silicon nanowires have demonstrated the ability to increase the CHF and the heat transfer coefficient by more than 100% [13].

Because of the impact it has on heat transfer applications, liquid propagation through structured surfaces (and hence surface wettability) is extensively studied in the past [17-23]. Xiao *et al.* [21] have demonstrated multi-layer spreading of a film of liquid water on superhydrophilic surfaces. They demonstrated that propagation of liquid on an array of nanopillars with scalloped features can separate into multiple distinct layers of liquid as shown in Fig. 1-2b. Multi-layer spreading of liquid helps to control the liquid thickness which is the main source of the conduction resistance which limits the heat transfer.

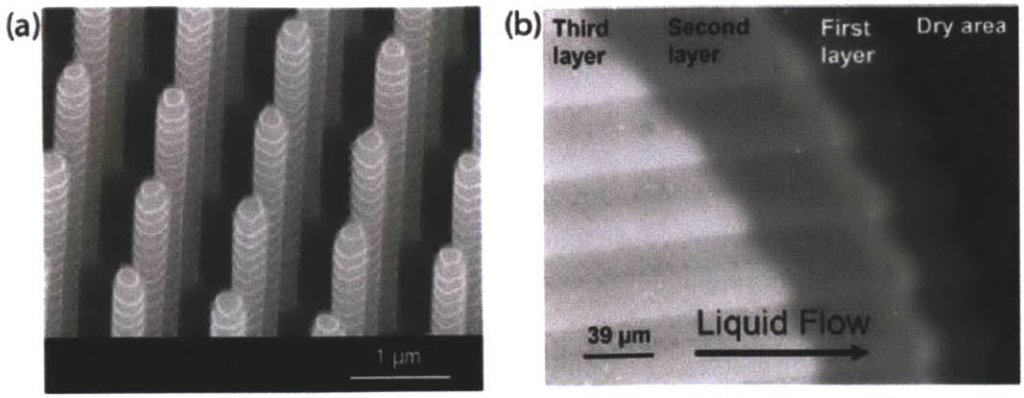

Figure 1-2: Scanning electron microscope (SEM) image of (a) silicon pillars with scallop feature, (b) visualization of multi-layer liquid spreading [21].

One concern in applications such as spray cooling which involve phase change is whether an impinging droplet will contact the solid surface and wet it or will it bounce back without actually touching the heated surface. Effective cooling requires wetting droplets. Hence, this thesis, we will discuss one of the challenges that hinder this endeavor of achieving higher heat flux removal rate: non-wetting droplets on superhydrophilic surfaces at superheated conditions.

1.2 Roughness and Wettability

Fundamental understanding of solid-liquid interactions is important to control surface wettability and design surfaces with superior wetting behavior. Whether or not a droplet would wet a flat rigid surface is determined by the force balance at the three phase contact line where the solid, liquid and vapor interfaces meet. Liquids have interfacial tension that acts to minimize the surface energy. This interfacial tension is expressed as energy per unit area or equivalently force per unit length. For ideal solid surfaces, which are both atomically smooth and chemically homogeneous, the force balance at the three phase contact line which determines the shape of a droplet is given by Eq. 1-1,

$$\gamma_{SV} = \gamma_{SL} + \gamma_{LV} cos\theta_Y, \tag{1-1}$$

where γ is the surface tension force which corresponds to the corresponding phases indicated by the index (S for solid, L for liquid, and V for vapor) and θ_Y is the Young angle (also called intrinsic contact angle). Young angle is dependent on the chemical nature of the different phases involved.

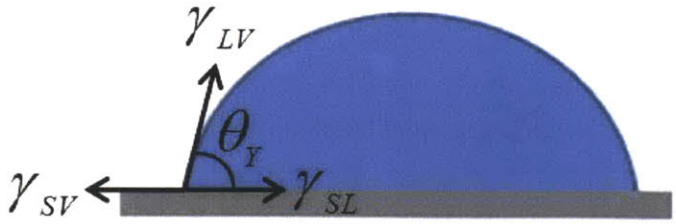

Figure 1-3: Classical force balance at the three phase contact line on a smooth surface.

When the Young angle is greater than 90°, the solid surface is called hydrophobic whereas the surface is termed as hydrophilic when the contact angle is less than 90° as shown in the Fig. 1-4. Water droplets spread on hydrophilic surfaces while they maintain their shape by not spreading in hydrophobic surfaces as shown in the schematic in Fig. 1-4.

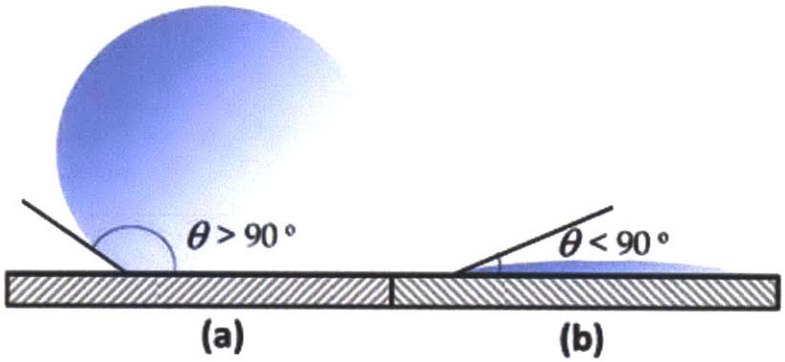

Figure 1-4: A schematic of a water droplet on a (a) hydrophobic and (b) hydrophilic surface.

A droplet will spread on the solid surface if the solid-vapor surface tension, which entrains the droplet, is larger than the sum of the solid-liquid and the liquid-vapor surface tension forces both of which resist the spreading of the droplet. The spreading coefficient which is denoted by S and given by Eq. 1-2 determines whether or not the droplet spreads for a given surface,

$$S = \gamma_{SV} - \gamma_{SL} - \gamma_{LV}. \tag{1-2}$$

When $S > 0$, the droplet will spread, where as it forms a hemisphere or a small lens when $S < 0$. If γ_{SL} is larger than $\gamma_{SV} + \gamma_{LV}$, the contact line will be withdrawn by surface tension forces until a film of air comes between the solid and the liquid, hence complete drying.

Wettability of surfaces can be tuned by introducing roughness, which alters the apparent contact angle [24, 25]. This effect has been demonstrated since the 1940 [26, 27] whereby texturing increases the degree of hydrophilicity of an inherently hydrophilic surface. Texturing also increases non-wettabilty by increasing the hydrophobicity of an inherently hydrophobic surface. Shibuichi *et al.* [28, 29] from the Kao Corporation demonstrated super water-repellent behavior with contact angles as high as 174° on fractal surfaces as shown in Fig. 1-5. They

compared the apparent contact angle (ACA) on the rough surface with the intrinsic contact angle on a smooth surface. To obtain a wider range of Young angles, the comparison was done on different liquids (hence different surface tensions). A typical result is displayed in Fig. 1-5 where the cosine of the apparent contact angle $cos\,\theta^*$ is plotted as a function of the cosine of the intrinsic contact angle $cos\,\theta$, showing the enhancement in the wetting behavior due to roughness.

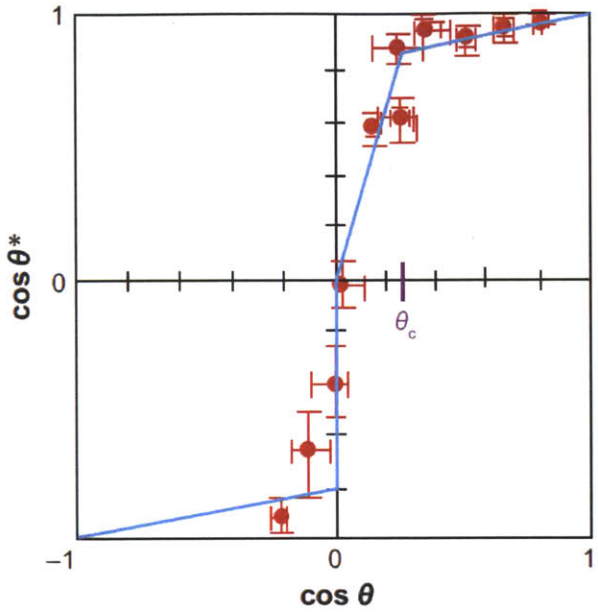

Figure 1-5: Effect or roughness on contact angle [30].

The experimentally obtained minimum data point on the x-axes in Fig. 1-5 was never smaller than -0.3 which corresponds to an intrinsic contact angle of approximately 110° emphasizing the Young angle on a flat solid to never exceed the maximum chemical hydrophobicity of a flat surface (120°). The corresponding apparent contact angle, however, reaches 170° which is much larger than the intrinsic contact angle. Roughness (or texturing) allows for a superior wetting behavior that could not be achieved otherwise.

In the hydrophilic domain (positive abscissa), the cosine of the apparent contact angle *cos* θ* first increases linearly with *cos* θ with slope greater than unity. This behavior, however, is not obeyed when the intrinsic contact angle becomes smaller than a critical value θ_c as shown in Fig. 1-5. Since the surface has already approached the limit of extreme wettability, texturing does not have significant effect in this domain. Instead a second linear regime with slope smaller than unity is observed in this domain. This domain is characterized by near zero contact angle and spontaneous spreading of droplets which are the characteristic features of superhydrophilic surfaces.

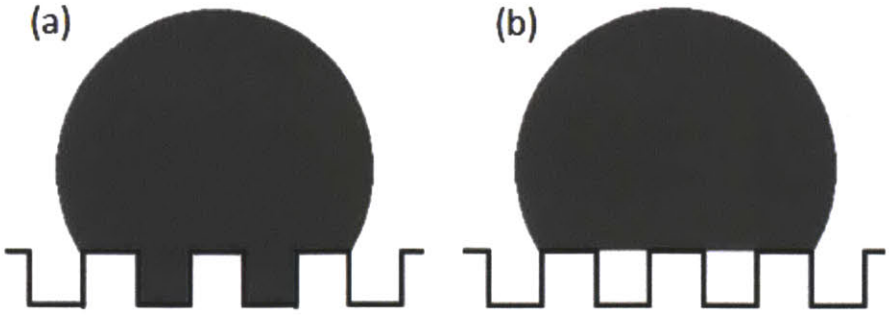

Figure 1-6: (a) Wenzel and (b) Cassie-Baxter droplet on a textured surface.

There are two classical models for predicting the apparent contact angle of rough surfaces as shown in Fig. 1-6: the Wenzel model [31] and the Cassie-Baxter model [32]. The Wenzel model is characterized by fully wetting of solid surface following surface asperities and the apparent contact angle is given by Eq. 1-3,

$$cos\ \theta^W = r cos\ \theta_Y, \tag{1-3}$$

where θ^W, θ_Y are the Wenzel and Young angles respectively, and r is the roughness which is defined as the ratio between the actual and projected surface areas. This equation is derived by minimizing the surface energy for a sessile droplet on a rough surface. The roughness which is usually greater than unity decreases the apparent contact angle if the Young angle is less than 90° (hence hydrophilic surfaces become more hydrophilic) and increases the apparent contact angle if the Young angle is greater than 90° (hence hydrophobic surfaces become more hydrophobic). This change in wettability is schematically shown in Fig. 1-7 where the arrows indicate the direction of change of the contact angle due to induced roughness. In the figure, the angle between the red line and the abscissa represents the ACA while the angle between the black line and the abscissa represents the intrinsic contact angle.

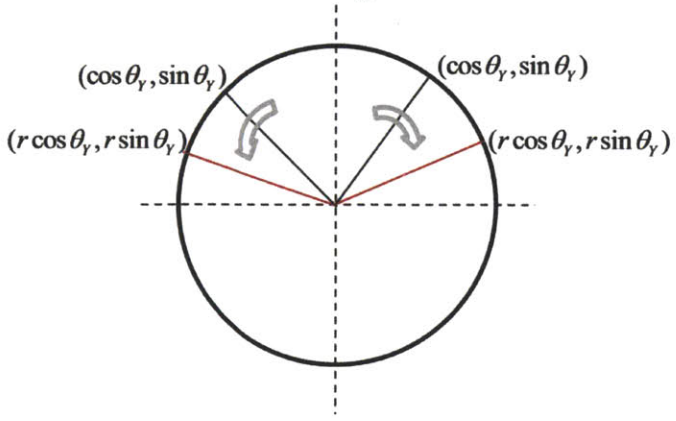

Figure 1-7: Effect of roughness on contact angle.

A droplet in the Cassie-Baxter state on the other hand sits on top of the rough structure with air trapped between the asperities and the droplet base [25, 30, 33]. Cassie-Baxter droplets

(also called Fakir droplets) do not wet the substrate and they have reduced area of contact with the solid substrate. The equation for the Cassie-Baxter model for heterogeneous surfaces is given by Eq. 1-4

$$cos\,\theta^{CB} = \phi_s cos\,\theta_{Y1} + (1 - \phi_s)\,cos\,\theta_{Y2}, \tag{1-4}$$

where ϕ_s is the area fraction of the solid-liquid interface and θ_{Y1} and θ_{Y2} are the respective Young angles of the composite surface. One of the components is air and droplets have a 180° contact angle in air. Hence the above equation is further reduced to Eq. 1-5

$$cos\,\theta^{CB} = -1 + \phi_s(1 + cos\,\theta_{Y1}). \tag{1-5}$$

Whether a droplet would be wetting or non-wetting depends on its history and the deposition technique [25, 33]. Broadly speaking, the wetting state with the lowest free energy is favored. However, metastable states are not uncommon. Patankar [33] used thermodynamics arguments to demonstrate that the droplet does not always exist in its lowest energy state. He showed that the state of the droplet (whether it's Cassie or Wenzel) depends on how the drop is formed and a droplet in the Cassie state will transition to the Wenzel state only if it overcomes an energy barrier. Cassie and Wenzel drops exhibit significantly different wetting characteristics and have been extensively studied in the past with special emphasis on understanding the transition between the two states [34-36].

The Cassie-to-Wenzel transition can be induced by applying external stimuli such as vibration, pressure, electric fields, or thermal excitation. Vibration-induced Cassie-to-Wenzel transition of droplets on rough surfaces was studied by Bormashenko *et al.* [37, 38]. They reported that the resulting force per unit length on the three phase contact line is responsible for the Cassie-to-Wenzel wetting transition and that the apparent contact angle is dictated by the interfacial interaction occurring at the three phase contact line. Han *et al.* [39] investigated the Cassie-to-Wenzel transition for a superhydrophobic carbon nanotube-based nanocomposite surfaces by applying a potential difference between the water droplet and the solid substrate (electrowetting). In another work, Krupenkin *et al.* [40] investigated both theoretically and experimentally the fully reversible wetting-dewetting transitions of droplets on electrically tunable superhydrophobic nanostructured surfaces. Also, the water infiltration dynamics during evaporation triggered wetting transition of a droplet from non-wetting to wetting state on transparent hydrophobic microstructured surfaces was studied by Tsai *et al.* [41]. They demonstrated that a naturally occurring evaporation process (without any external stimuli other than being exposed to the ambient) can drive the wetting transition in hydrophobic miscrostructured surfaces if the droplets are below a few hundreds of micron in radius. Zhang *et al.* [42] experimentally studied the effect of temperature on the wetting transition of droplets from spreading (wetting) to bouncing (non-wetting) on micro- and nanostructured surfaces.

In this thesis, we will show that superheat is another factor that plays a role in determining whether a droplet would wet or not wet a structured surface. We will demonstrate this dependence of wetting behavior on surface superheat by carrying out experiments at different superheats and observing whether or not droplets wet the surface. The study offers a new perspective on the wetting behavior of droplets at superheated conditions.

1.3 Motivation

Following the recommendations suggested by previous works to enhance liquid spreading on structured surfaces [22], we used photolithography and deep reactive ion etching to fabricate silicon micropillar square array structures with varying diameter, height, and center-to-center spacing of 2-5, 20-35 and 10-35 μm, respectively. Experiments were carried out to investigate liquid spreading on these well-defined structured surfaces. While droplets typically spontaneously spread and wet the surface upon touching the solid substrate at room temperature with near zero contact angle, we observed that some droplets do not wet the surface. Instead they sit on top of the pillar array structure with apparent contact angles in excess of 160° due to induced evaporation at superheated conditions as shown in Fig. 1-8. However, the non-wetting droplets wet the surface when the surface superheat is reduced significantly.

Understanding this shift in wettability due to change in surface superheat will provide insight to the wetting dynamics of droplets which will be useful to phase-change heat transfer processes such as evaporation, spray cooling and jet impingement. Hence, the focus of this thesis is to experimentally investigate:

(a) the effect of superheat on surface wettability,
(b) non-wetting droplets on superhydrophilic surfaces at superheated conditions, and
(c) the steady state transition of droplets from non-wetting to wetting state at superheated conditions.

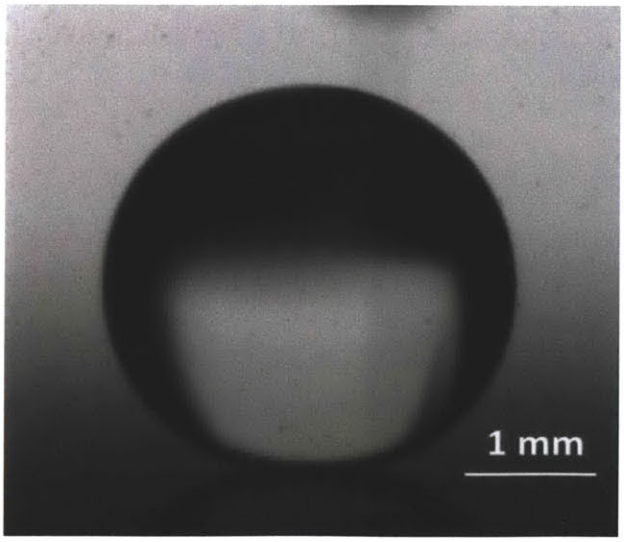

Figure 1-8: A non-wetting droplet on a superhydrophilic surface at superheated conditions.

1.4 Thesis Objective and Outline

In this thesis, we will experimentally investigate non-wetting water droplets on superhydrophilic surfaces at superheated conditions.

In *chapter 1*, a general overview of the different cooling techniques along with their pros and cons was presented. The effect of roughness on wettability, liquid spreading, and phase-change heat transfer processes were briefly discussed. Moreover, the different states of a droplet and the associated wetting transitions of one state to another on a structured surface were discussed.

In *chapter 2*, the design and microfabrication process of the test samples will be discussed.

In *chapter 3*, steps prior to acquiring experimental data (such as sample preparation and temperature sensor calibration) are presented. The experimental methodology is presented in detail along with temperature measurement and control. Lastly, measurement uncertainties of the parameters of interest are briefly discussed and quantified.

In *chapter 4*, experimental data are presented and discussed. Effects of superheat and droplet size on the observed phenomenon are discussed and a correlation is drawn from experimental observation.

In *chapter 5*, a 1-D lubrication type model that captures the physical phenomenon is presented. The assumptions that are made in developing the model are discussed and verified. Moreover, the relevant forces that are involved in the phenomena are derived from first principle. Lastly, experimental data are plotted against model prediction for comparison. The discrepancies between experimental data and model prediction are highlighted and discussed.

In *chapter 6*, conclusions are drawn and recommendations for future work are proposed following the discussion on the contributions of this work.

In *appendix*, the microfabrication procedure is revisited in a step by step manner in a tabular form. Moreover, a custom made MATLAB script that is used to plot the model prediction is presented for completeness.

CHAPTER 2

2. Microfabrication

The structured surfaces used for studying evaporation-induced non-wetting droplets were manufactured using projection lithography and deep reactive ion etching at the Microsystems Technology Laboratory at Massachusetts Institute of Technology. The structured surfaces were designed using L-edit. The details of the design are presented in section 2.1 and the fabrication procedure is discussed in detail in section 2.2.

2.1 Sample Design

The contact lithography masks used to define the microstructured pillar array geometry on the front side, and the resistive heaters and the temperature sensors on the back side which were designed using L-edit (Tanner Research Inc.) are shown in Fig. 2-1. The dimension of the structured surface on the front side of the test sample is 35 mm long by 10 mm wide whereas the overall dimension of the test sample is 40 mm long by 20 mm wide. The 5 mm extra space on the edge is used for external connection and handling. The line width of the heating wires was 350 μm and the heater covers the structured surface.

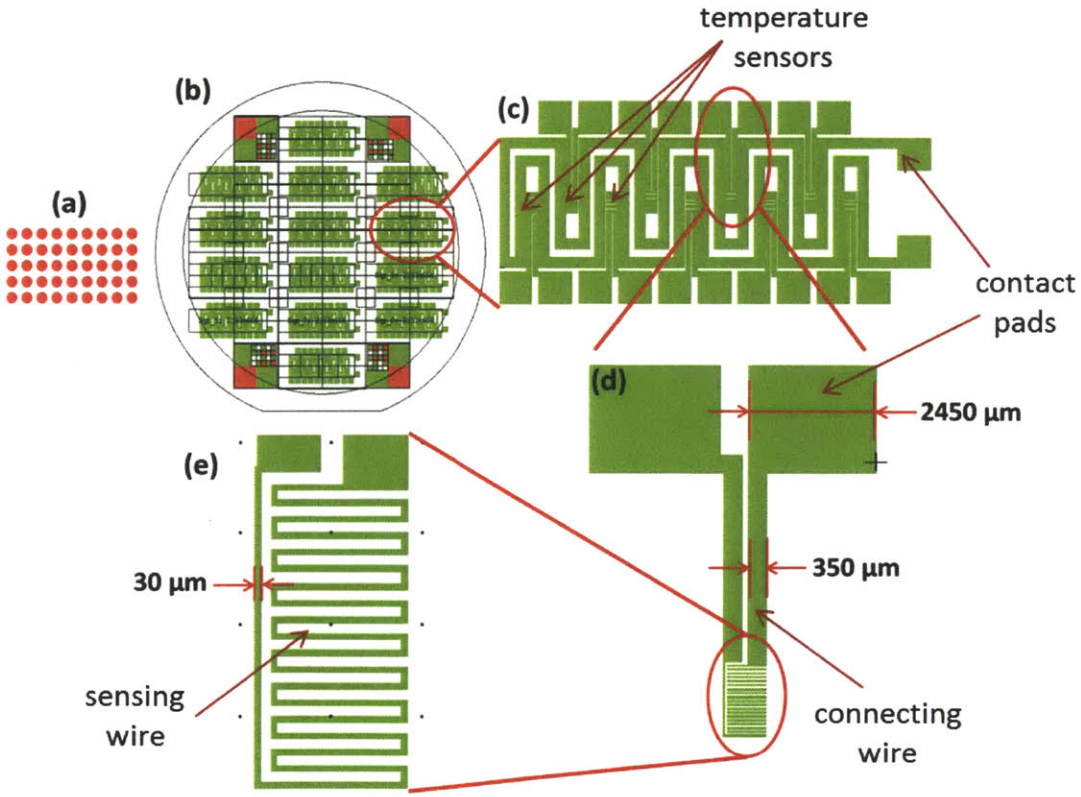

Figure 2-1: L-edit design (a) front pillar layout, (b) back heater layout, (c) heater design, (d) temperature sensor design, (e) temperature sensor detail.

Nine equally spaced (3 mm apart) temperature sensors lying along the center line of the test sample were used to measure the local temperature. They were used as resistance temperature detectors (RTDs). The line width of the sensing wire (30 μm) was smaller than the line width of the connecting wire (350 μm) as shown in Fig. 2-1d-e. This was done to ensure that the majority of the excitation voltage drop occurs in these wires. This indicates that the temperature sensors measure the local temperature. All the contact pads have the same dimension (2450 x 2450 μm^2). Moreover, all the wires including the contact pads have the same thickness (~ 200 nm) which was determined during the electron beam (ebeam) evaporation process in the fabrication step as will be discussed in the microfabrication section.

2.2 Microfabrication

A 150 mm diameter double side polished silicon wafer bought from Wafernet, Inc. (wafernet.com) was used to manufacture various test samples with varying pillar diameter D, height H, and center-to-center spacing L of 2-5, 20-35 and 10-35 μm respectively at the Microsystem Technology Laboratory (MTL) at MIT using photolithography and deep reactive ion etching (DRIE).

Before starting the fabrication process, the wafer was RCA cleaned which was followed by a 200 nm thermal oxide growth in a tube. The next step in the manufacturing process was photolithography. A resist was spun on the front side of the wafer after priming the wafer in an HMDS (Hexamethyldisilazane) oven. The wafer was then prebaked, ultraviolet (UV) exposed, developed, and finally postbaked in an oven. The hardened photoresist that remained on top of the pillar array structure together with the oxide layer underneath it was used as a mask for the DRIE process. The height of the pillars was determined at this stage by varying the etching time. Piranha removed the resist while reactive ion etching (RIE) was used to strip off the remaining oxide layer from the top of the pillars. A schematic of the process steps for the front pillars is shown in Fig. 2-2.

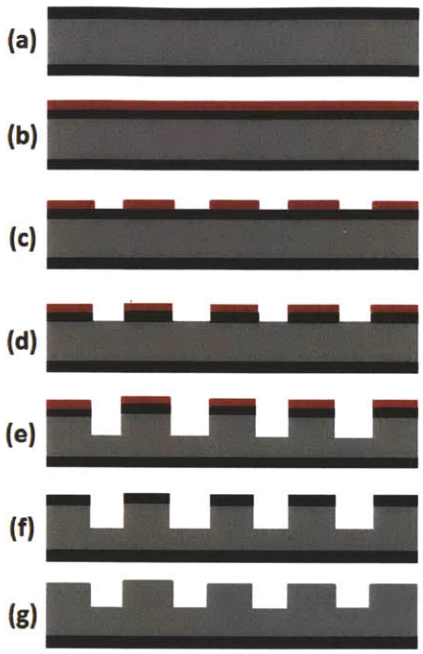

Figure 2-2: Schematic of the front fabrication process: (a) thermally grown oxide layer, (b) spin coat resist, (c) pattern and develop, (d) RIE, (e) DRIE, (f) piranha, (g) RIE.

After completing the steps shown in Fig. 2-2, the wafer was positioned upside down to start printing the resistive heaters and the temperature sensors at the back side of the wafer. The heater and the temperature sensors were integrated and each test sample has its own heater with nine evenly spaced temperature sensors. The back side of the wafer was spin coated with a resist after HMDS. The resist was then prebaked, UV exposed, postbaked, flood exposed and finally developed. Ebeam evaporation was then used to deposit a 200 nm thick gold layer. Since gold does not stick well onto oxide layer, a 20 nm seed layer of chromium was used to assist the adhesion. The ebeam evaporation was followed by acetone lift-off. The last step in the fabrication process was dicing the wafer into the appropriate size (20 mm by 40 mm) using a diesaw. This step completes the back side process which was used to create the heaters and sensors. The schematic of the back side process is shown in Fig. 2-3.

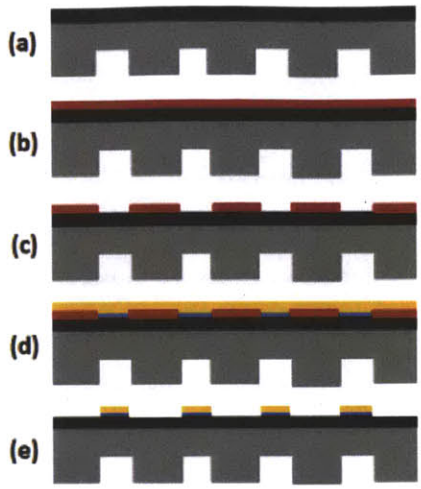

Figure 2-3: Schematic showing the back side fabrication process: (a) oxide layer, (b) spin coat resist, (c) pattern and develop, (d) ebeam evaporation, (e) acetone lift-off.

Due to limitations in the fabrication process, the pillars were not the same size as the photomask design. Therefore, actual measurement using scanning electron microscope (SEM) was necessary after completion of the fabrication process. A typical SEM image from which pillar dimensions (diameter, height, and center-to-center spacing) were deduced is shown in Fig. 2-4. The height of the pillars was obtained by taking measurements at a tilted position as shown in Fig. 2-4b.

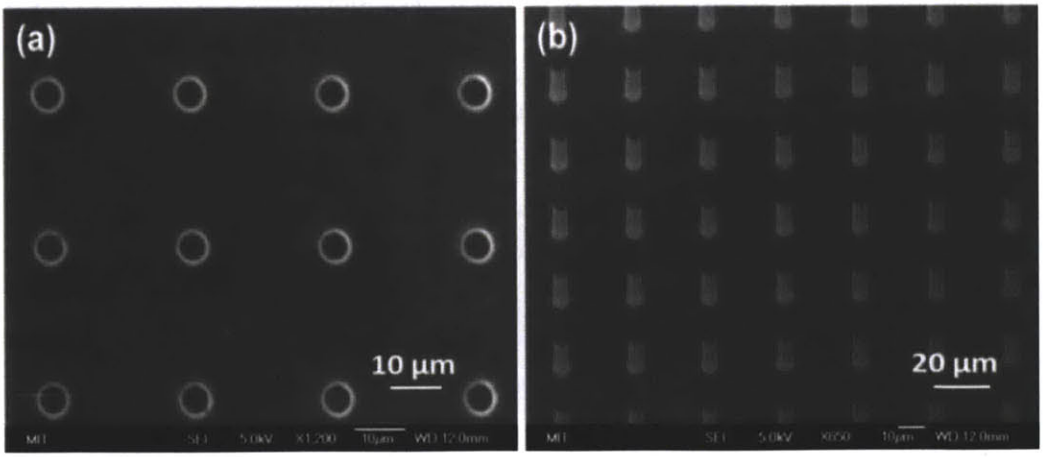

Figure 2-4: SEM image of (a) top (b) 30° inclined side view of a typical microstructured surface with D = 5.2 µm, L= 28.0 µm, and H = 22.2 µm.

Figure 2-5 shows the front and backside of a typical test sample after completing the fabrication process. The temperature sensors require calibration before using them as RTDs. A fixture which was used to hold the test sample was manufactured from Teflon (PTFE) at the Central Machine shop at Massachusetts Institute of Technology.

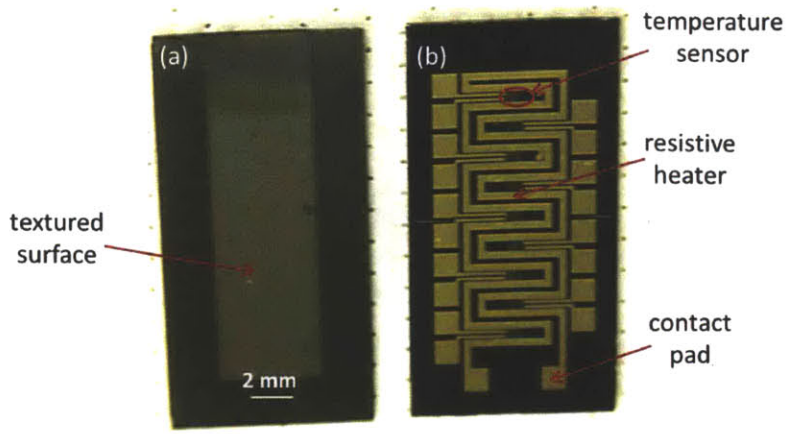

Figure 2-5: Image of a typical test sample (a) microstructured front side (D = 5.2 µm, L= 28.0 µm, H = 22.2 µm) (b) back side showing the resistive heater and temperature sensors.

2.3 Summary

A photomask was designed using L-edit. Photolithography and deep reactive ion etching were used to fabricate well-defined silicon pillar arrays in a square pattern. The pillar diameter, height, and center-to-center spacing were varied from 2-5, 20-35 and 10-35 µm, respectively. The pillar diameter and the center-to-center spacing were determined in the photomask design stage while the pillar height was determined during the deep reactive ion etching process by varying the etching time. Due to manufacturing limitation, SEM images were necessary to verify the actual geometric dimensions of the pillar array structure.

A resistive heater and nine evenly spaced temperature sensors were integrated to the back side of the test sample using ebeam evaporation and acetone lift-off processes. The heaters and sensors were made from gold. Gold does not stick well onto oxide layer. Hence, to assist the adhesion a 20 nm chromium layer was applied as a prime layer. After completing the front and back side fabrication steps, the wafer was diced into appropriate dimension (20 mm by 40 mm) using a diesaw. The packaging completes the sample fabrication process.

CHAPTER 3

3. Experiment

Custom made temperature sensors which were integrated with the back side resistive heater were used to measure the local temperature of the test sample. These temperature sensors required calibration before using them as resistance temperature detectors (RTDs). We will discuss the calibration procedure and the associated problem of resistance drifting in section 3.1. That discussion will be followed by procedures carried out to prepare the samples for experiment. Section 3.3 presents the experimental set up used to carry out the experiment. The chapter concludes by discussing the measurement uncertainty of the parameters of interest in section 3.4 followed by a brief summery.

3.1 Temperature Sensor Calibration

The integrated temperature sensors that were printed at the back side of the test sample were designed to function as RTD. RTDs are sensors that are used to measure temperature by correlating the resistance measurement with an equivalent temperature since resistance is a function of temperature. They function by passing a low-level voltage (also called excitation voltage) and measuring the voltage drop across the sensor. Hence, they required calibration prior to use to relate the resistance with temperature.

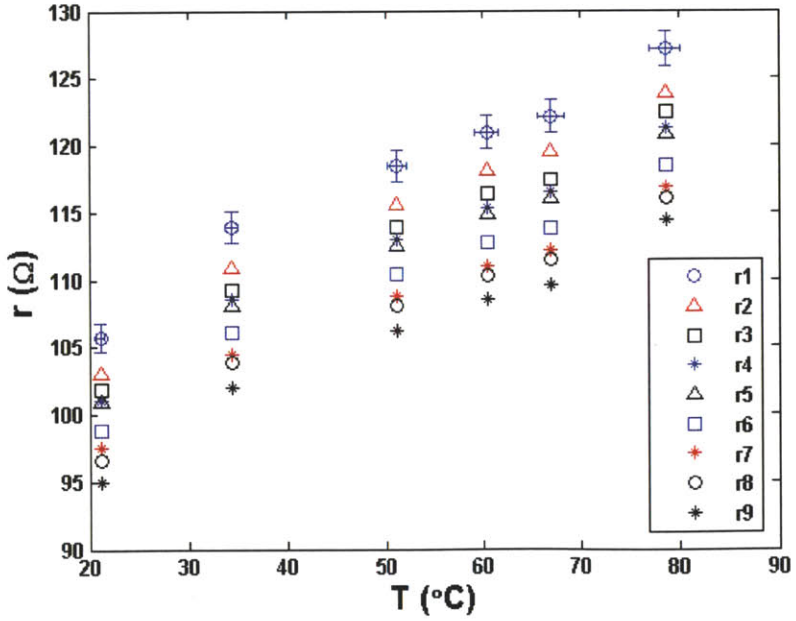

Figure 3-1: Sensor resistance as a function of temperature.

Each temperature sensor was calibrated individually in a conventional oven before experiment. A typical calibration curve is shown in Fig. 3-1 where the x- and y-axis represent the temperature in °C and the resistance in Ω, respectively. Temperature and resistance data were

obtained at a 30 Hz rate using a data acquisition card (DAQ6036E, NI) during calibration. Using a statistical approach, we calculated the standard deviation of the temperature and resistance data and found out that the maximum percentage error for the temperature and resistance data were less than 2% and 1% respectively. Hence, we used a conservative estimate of 2% and 1% for temperature and resistance readings respectively to produce the error bars shown in Fig 14.

Extra care was taken during the calibration step by verifying the oven temperature independently. The oven has its own built in thermometer. The correctness of the reading of this thermometer was verified by measuring the oven temperature using an independent RTD. When both readings from the thermometer and RTD reached steady state values, the temperature was noted and the resistance of each sensor was measured indirectly by measuring the voltage drop across each sensor. This step was repeated at different steady state temperatures as shown by the data points in Fig. 3-1. Above 100 °C, the wires connecting the sensors started melting and hence no data was obtained above 80 °C. However, as demonstrated in Fig. 3-1, the calibration curves were linear in nature, and hence the plot was extrapolated for higher temperatures above 100 °C. The relationship between the sensor resistance r in Ω and the substrate temperature T in °C can be expressed by Eq. 3-1

$$r(T) = r_0 + \alpha T, \tag{3-1}$$

where r_o is the y-intercept in Ω and α is the slope of the line in Ω/°C (Fig. 3-1). The slope and the y-intercept that are obtained from the linear regression curve are matched with Eq. 3-1 to deduce the numerical values of r_o and α.

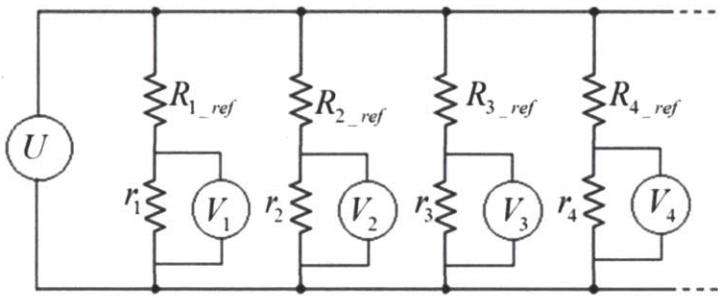

Figure 3-2: Circuit diagram of the temperature sensors.

The circuit used for calibrating the temperature sensors is shown in Fig. 3-2. Each temperature sensor was connected in series with a reference resistor and the combination was connected in parallel with each other. The entire circuit was connected to a common DC power source (E3632A, Agilent). All reference resistances (R_{i_ref}) were measured prior to building the electric circuit network and the values were checked against the color code. The overall voltage (U) and the voltage drop across each sensor (V_i) were measured using LabView 8.5. These sets of data (U and V_i from LabView and R_{i_ref} from actual measurement of the reference resistance) were entered into the custom made LabView script which computed the resistance of the individual sensors (r_i) using Eq. 3-2,

$$r_i = \frac{R_{i\_ref}}{\left(\frac{U}{V_i} - 1\right)}. \tag{3-2}$$

Equation 3-2 gives us the values in the y-axes at a known steady state temperature. This completes the calibration step and we have successfully correlated the resistance of the temperature sensors and the steady state temperature by producing Fig. 3-1. The temperature sensors are located 3 mm apart and their location on the test sample is shown in Fig. 3-3.

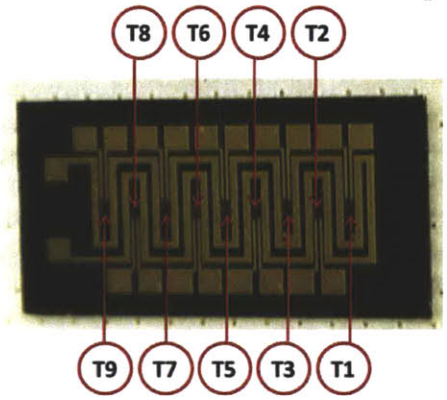

Figure 3-3: Temperature sensor location (nine temperature sensors).

We used the same circuit that was previously used for calibration to measure temperature during actual experiment. As was done for calibration, we measure the common voltage supply U and the voltage drop across each sensor V_i. The reference resistance R_{i_ref} is known, and the slope α and the y-intercept r_o are known after successfully completing the sensor calibration. Hence, we were able to obtain the temperature of the test sample during experiment by using Eq. 3-3 which is obtained by equating Eqs. 1 and 2 and solving for T (all quantities are known or measured except the temperature)

$$T = \frac{1}{\alpha}\left[\frac{R_{i\_ref}}{\left(\frac{U}{V_i} - 1\right)} - r_0\right]. \tag{3-3}$$

However, the sensor resistance had noticeable drift during the experiment. This problem was detected by measuring the resistance of the temperature sensors before and after experiment as shown in Fig. 3-4 where a significant resistance drift is experimentally measured. The resistance drifting made the temperature reading obtained from Eq. 3-3 erroneous. All temperature sensors drifted upward which resulted in false reading (temperatures readings were higher than the true value).

This amount of the resistance drift increased with the duration of the experiment and substrate temperature. A longer experiment at a higher temperature showed the biggest drift

while small drifting was observed for short experiments at lower temperature. Once we identified the problem, we tried various annealing techniques to solve it. However, the problem persisted and hence T-type thermocouples were used for temperature measurement afterwards.

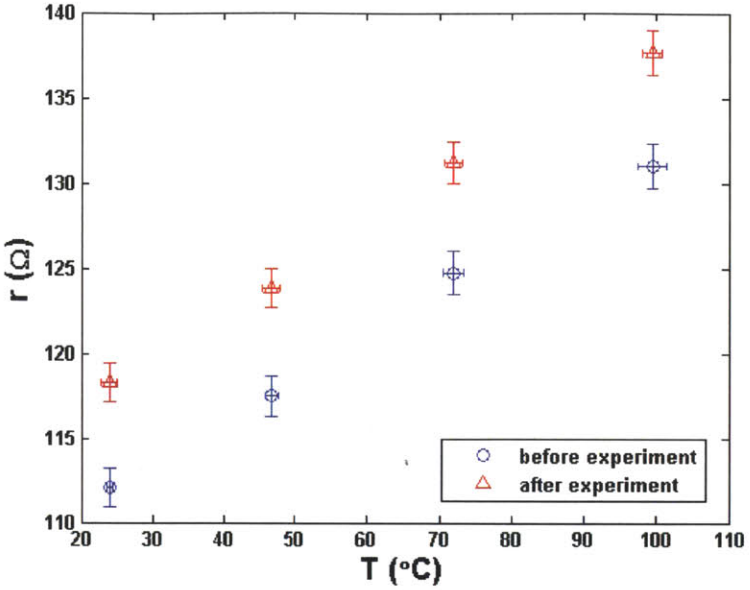

Figure 3-4: Typical resistance drifting of temperature sensors.

3.2 Sample Preparation

Before starting the actual experiment, the samples were cleaned with acetone, methanol, isopropanol (IPA) and deionized (DI) water; dried with nitrogen gas; and then oxygen plasma treated for 30 minutes to remove organic contaminants. After plasma cleaning, the surface becomes superhydrophilic and droplets spontaneously spread on the surface with near zero contact angle. The water was allowed to boil before experiment to remove dissolved gases. Hence, thoroughly degassed DI water was used for all experiments to avoid early bubble nucleation. The samples were positioned horizontally with the structured surface facing up the droplet. A resistive heater was used to heat the sample from the back side using a DC power source. A pipette was used to gently dispense droplets of volume 15-25 μL on the heated substrate on top of the structured surface. A 25 μm diameter gold wire, functionalized in a 1 mM ethanol solution of 1H, 1H, 2H, 2H-perfluorodecanethiol (Sigma-Aldrich), was used to keep the highly mobile droplets in position for visualization. The thiol coating made the intrinsically wetting gold wire hydrophobic to reduce the force by which it attracts the droplet upward.

The wall temperature of the substrate was measured and recorded at a rate of 10 Hz using a T-type thermocouple (TC) which was attached to the backside of the test sample using thermal grease (3G Cool Silver, AI Technology) and Kapton tape. This procedure was devised since the integrated temperature sensors were erroneous due to resistance drifting (see section 3.1). The TC was attached to data acquisition card (DAQ6036E, NI) which interfaced with LabView 8.5. The LabView used a built-in function to measure temperature. In order to visualize the

phenomena, images were also acquired at 10 fps. The image and temperature data were later synchronized to closely investigate the wetting dynamics of droplets.

3.3 Experimental Setup

The test sample was positioned horizontally with the textured surface facing up the needle which dispensed the droplet as shown in Fig. 3-5. While droplets typically spontaneously spread and wet the surface upon touching the solid substrate at room temperature, we observed that water droplets do not wet the structured surface when the surface was heated beyond a critical superheat. Above this critical superheat, liquid propagation on the surface ceases and non-wetting droplets on pillar tops were observed.

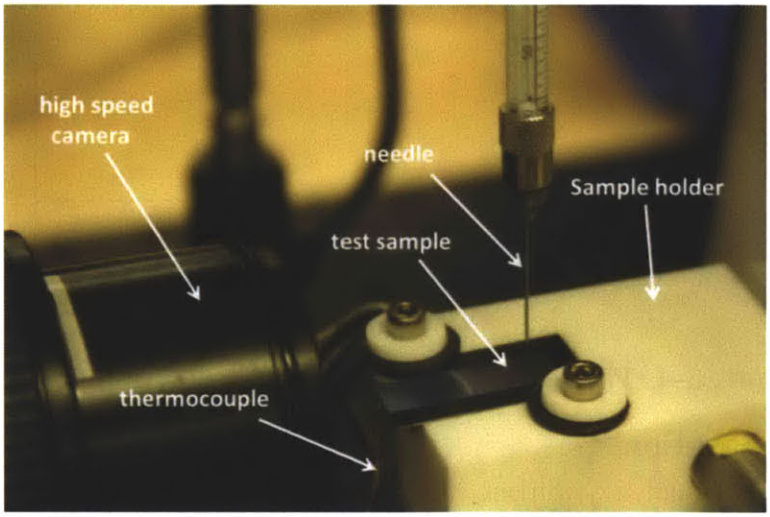

Figure 3-5: Experimental setup.

In this simple experimental set up, we obtained the temperature from the TC reading and the images were captured using a high speed camera (Phantom 7.3, Vision Research). Important parameters of interest such as droplet volume, droplet diameter and apparent contact angle were obtained by post processing the captured images using a custom analysis routine written in MATLAB. Steady state temperature readings were obtained from the recorded data using a DAQcard. A typical image of a droplet used to obtain important parameters of interest is shown in Fig. 3-6. The apparent contact angle (θ_{app}) as measured from the inset image was 149° ± 2°. Also shown in the inset image are the pillars onto which the droplet rested. The pillars underneath the droplet are not visible due to the shadow casted by the droplet and the optical limitation we experienced in the experimental setup.

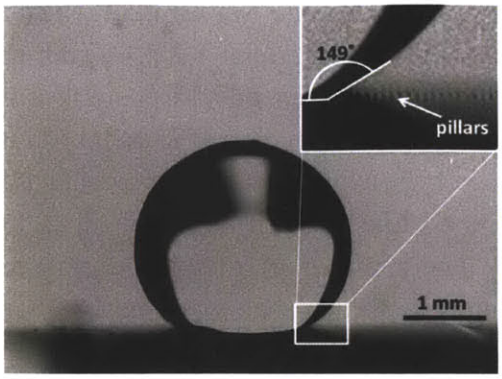

Figure 3-6: Image of an evaporating water droplet on top of a pillar array structure. The inset image shows the micropillars and apparent contact angle.

During experiment, we have observed that the superheat required to suspend a non-wetting droplet (> 75˚C) on top of the structured surface was significantly higher than that required to sustain the non-wetting state of an already deposited droplet (< 35˚C). This observation necessitated to devise a strategy that would allow the substrate to be maintained at two different steady state superheats: an initial higher steady state superheat at the initial deposition stage (start of the experiment) and a relatively lower steady state superheat to maintain the non-wetting state after deposition. This was accomplished using a proportional–integral–derivative controller (PID controller) and solid state relay (SSR) as demonstrated by the experimental setup shown in Fig. 3-7.

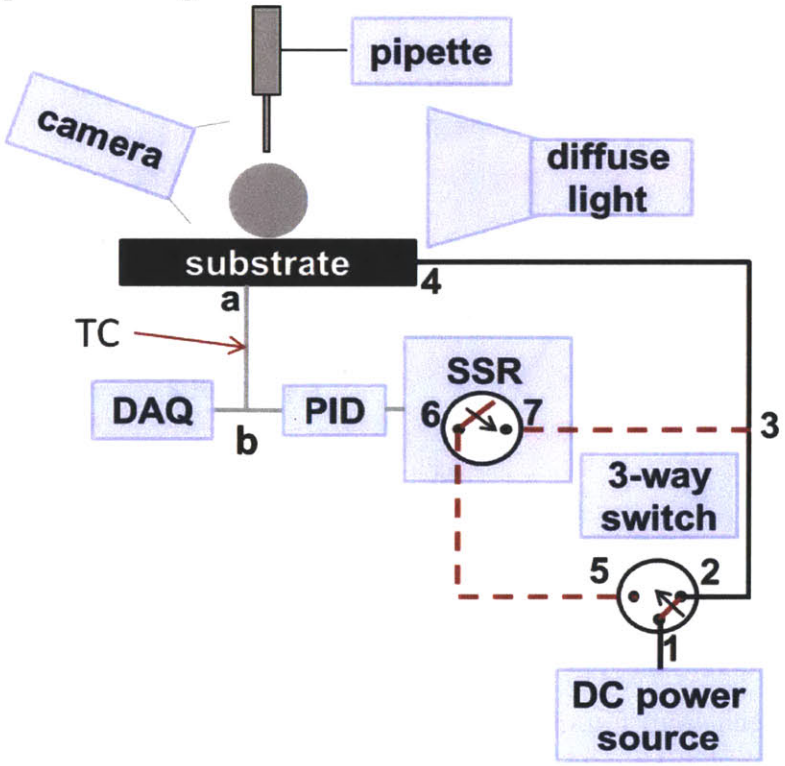

Figure 3-7: Schematic of a closed loop temperature feedback control system. The grayed fuzzy line a-b represents a thermocouple wire.

As shown in Fig. 3-7, the substrate was initially heated by a direct power supply overpassing the PID controller through junctions 1-2-3-4. This will establish the higher steady state superheat that was required for successfully depositing a non-wetting droplet on to the structured surface. Once the droplet was deposited on the substrate, the superheat was lowered by toggling the three-way switch from junction 2 to 5 such that the PID controller will be in control of establishing the second lower steady state superheat by controlling the current flow through junction 1-5-6-7-3-4. The circuit uses a closed loop system with temperature feedback where the substrate superheat is continuously monitored by the PID controller. Based on the temperature reading from the thermocouple a-b, the PID controller sends a pulse signal to the SSR. The SSR opens and closes the circuit at junction 6-7 in response to the pulse signal received from the PID controller. When the reading from the TC is higher than the temperature set on the PID controller, the SSR opens the junction 6-7 to stop any further heating. This lowers the substrate temperature since it starts cooling immediately. When the temperature reading from the TC drops below the temperature set on the PID controller, the PID controller sends a pulse signal to the SSR which in turn closes the junction 6-7 to complete the circuit. This on and off operation of heating power establishes the second lower steady state superheat at which we want to study the wetting transition of droplets. A typical temperature plot as a function of time that shows the two steady state temperatures is shown in Fig. 3-8. The first steady state superheat was established before depositing the droplet on the surface ($t<0$) and hence only a smaller portion of it is shown in Fig. 3-8 since this figure shows the superheat as a function of time after depositing the droplet.

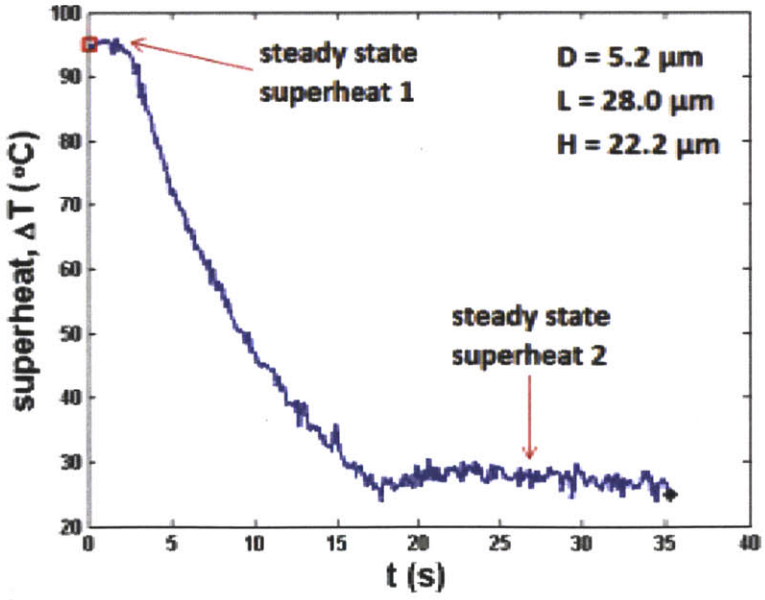

Figure 3-8: Typical superheat data showing the two steady state superheats.

As can be seen from Fig. 3-8, a 94 °C superheat was required initially to successfully deposit a non-wetting droplet onto the structured surface. However, only a 26 °C superheat was required to maintain the non-wetting state. This is because the forces that are involved during the

initial stage of droplet deposition are different from the forces that are involved afterwards. During deposition, the center of gravity of the droplet decelerates rapidly initiating a shock wave that propagates through the body of the droplet as depicted pictorially in Fig. 3-9. The shockwave envelope that results from the deceleration causes a reaction force that induces an enormous pressure that in effect pushes the droplet down onto the substrate, hence wetting pressure force [43]. This pressure is called water hammer pressure and it scales with the time derivative of the inertia term in the Navier-Stokes equation [44, 45]. The resulting force due to water hammer effect pushes the droplet down causing premature wetting. Water hammer pressure scales with the speed of sound in water (approximately 1500 m/s). This is the reason that necessitated two steady state temperatures: one at the beginning of the experiment to avoid premature wetting (usually higher) and another one to observe the steady state transition of droplets. The concept of water hammer pressure is an active area of research and the effects are not yet well understood.

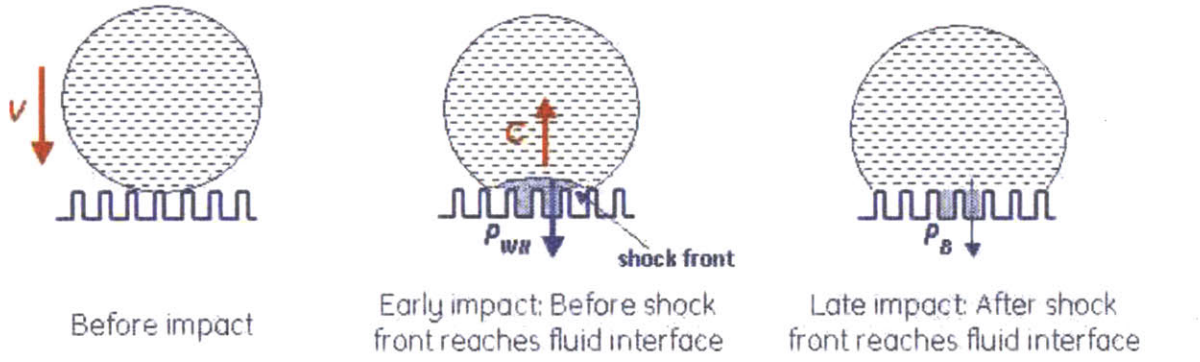

Figure 3-9: Sequence of events during droplet impact (water hammer pressure) [43].

3.4 Measurement Uncertainty

Temperature data were acquired at a rate of 10 Hz using a built in function in LabView. To quantify the error associated with the temperature measurement, 20 experiments were randomly selected and analyzed. The standard deviation of the collected data was combined with the error from using the TC. The uncertainty of the TC as given by the manufacturer is 0.75% of the reading or ±1 °C whichever is bigger. The maximum combined percentage error we calculated for the randomly selected data was 2.0 %. Hence, a conservative error estimate of ± 2.0 % of the reading was used to produce the error bars for the superheat. Figure 3-10b shows the temperature fluctuation from which the standard deviation was computed.

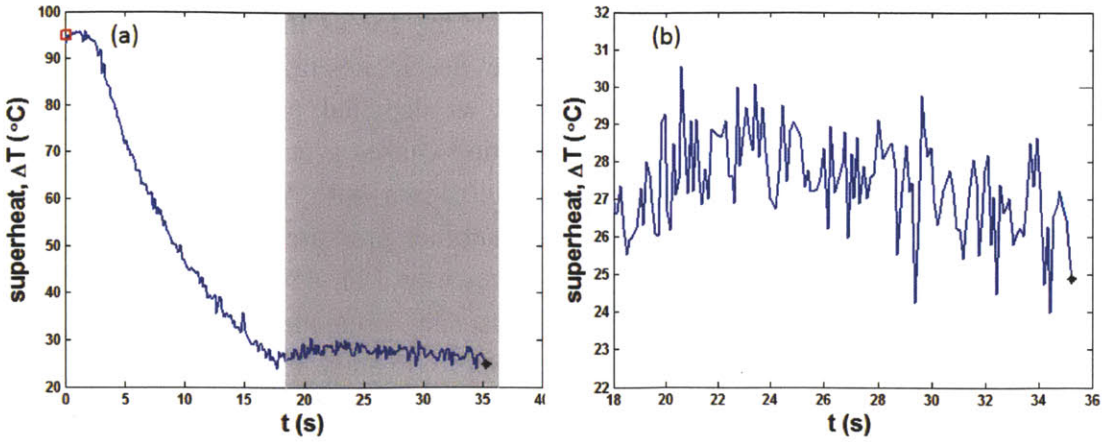

Figure 3-10: (a) Superheat as a function of time of an evaporating water droplet, (b) a closer look of the steady state superheat (grayed region from Fig. a).

The transition volume of the droplet was measured from the captured images. A MATLAB script was used to calculate the major diameter D, base diameter d, and height of the droplet from the base H from the images. Then, the script further calculates the volume of the droplet using two different formulas that uses different input parameters as shown by the Eqs. 4 and 5. The first method uses the major diameter and base diameter (Eq. 3-4) while the second method uses the droplet height and base diameter (Eq. 3-5). The dimensions D, d and H are shown schematically in Fig. 3-11. Finally, the MATLAB script calculates both volumes (V_I and V_{II}) and outputs the arithmetic mean V (Eq. 3-6) of the two volumes as the true droplet volume.

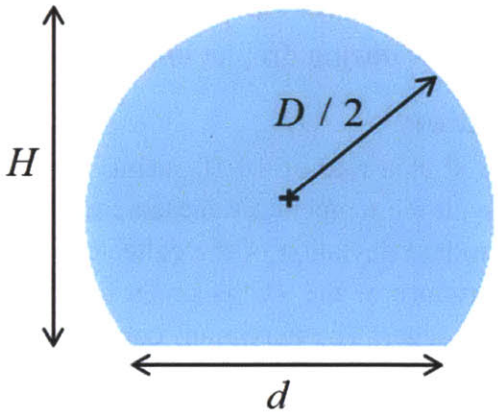

Figure 3-11: Schematic of a droplet showing major diameter, base diameter, and height.

$$V_I(D,d) = \frac{\pi}{12}D^3 + \frac{\pi}{8}D^2\sqrt{D^2 - d^2} - \frac{\pi}{24}(D^2 - d^2)^{3/2}, \tag{3-4}$$

$$V_{II}(H,d) = \frac{\pi}{6}H\left[3\left(\frac{d}{2}\right) + H^2\right], \tag{3-5}$$

$$V = \frac{1}{2}(V_I + V_{II}). \tag{3-6}$$

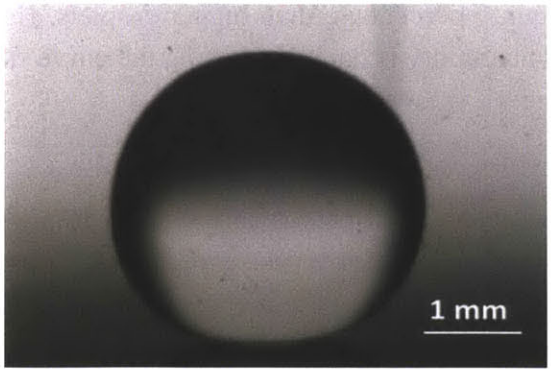

Figure 3-12: A typical image used by MATLAB to compute droplet volume.

To quantify the volume uncertainty, six experiments were selected randomly. For each experiment, V_I, V_{II}, and V are obtained by running the MATLAB script ten times. Percentage error was then computed for each experiment by combining the standard deviations of the two volumes (V_I, V_{II}) and the results are shown in Table 3.1 and Fig. 3-13. The error due to pixel count was orders of magnitude less than the error that resulted from the standard deviation of V_I and V_{II}.

Table 3.1: Summary of percentage error in volume.

Experiment	V (μL)	percentage error (%)
1	10.4	5.2
2	3.4	18.0
3	6.2	12.1
4	7.0	11.4
5	2.2	23.4
6	8.1	9.5

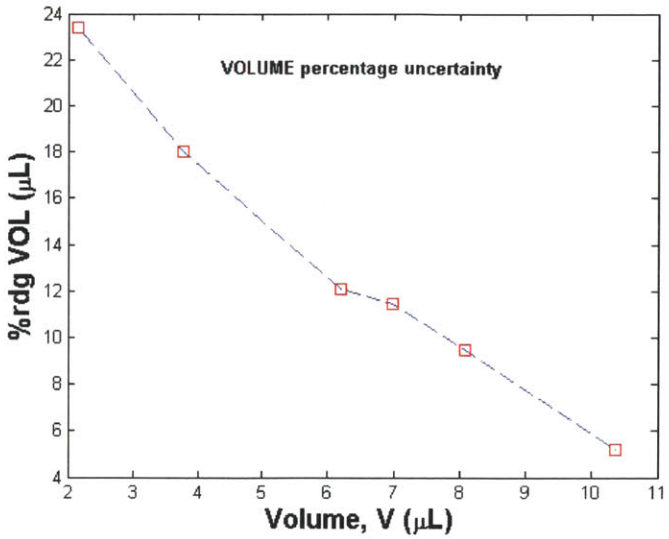

Figure 3-13: Relative percentage uncertainty of volume as a function of droplet size.

The percentage uncertainty varies with droplet size as shown in Fig. 3-13 *i.e.* smaller droplets have higher uncertainty percentage than bigger droplets. Hence, the above data is curve fitted linearly and volume uncertainty is computed using the curve fitting equation to produce the error bars for droplet volume.

3.5 Summary

Non-wetting droplets were observed to reside on superhydrophilic surfaces due to induced evaporation at elevated superheats. Moreover, experimental observations revealed that the droplets become wetting when the substrate superheat is lowered. To investigate this change in wettability, textured test samples with heater and temperature sensors at the back side are fabricated. The temperature sensors which were integrated with the back side resistive heater required prior calibration. The calibration curve was linear allowing extrapolation. However, due to resistance drifting of the sensors, the temperature reading was erroneous. As a result, the temperature sensors were replaced by T-type thermocouples to measure the substrate temperature.

Experiments performed at steady state superheats have shown that a higher superheat is required for initial deposition of a non-wetting droplet than the superheat required to maintain the state. The higher superheat required for the initial deposition is hypothesized to be the result of transient effects such as water hammer pressure. Due to this, two steady state superheats were required to carry out the experiment. This requirement necessitated the use of a closed loop temperature feedback system that used a PID controller, SSR and a three-way switch to establish the lower steady state superheat while the higher steady state superheat was obtained by direct heating of the substrate. The PID controller continuously monitors the substrate temperature and sends a pulse signal to the SSR. The SSR opens and closes the circuit based on the signal received from the PID controller which in effect establishes a steady state superheat. Then the wetting transition of droplets was studied at steady state conditions.

A conservative 2.0 % reading uncertainty is used to produce the error bars for the steady state superheat. However, we could not use a single percentage uncertainty for transition volume since the percentage error for smaller droplets was found to be higher than the percentage error for bigger droplets. Therefore, the uncertainty in the droplet volume is calculated based on the results found from the randomly selected representative volumes and the error bars are produced from the equation obtained by curve fitting the sample data.

CHAPTER 4

4. Experimental Results and Discussion

Superheat is observed to be one of the factors that determine whether a droplet would wet or not wet a structured surface. Experimental observations revealed that there exists a critical superheat above which all droplets remain non-wetting whereas 100% of the droplets wet the surface when the surface superheat was kept below the critical superheat. This necessitated further investigation, and in this chapter, we will present the change in the wetting behavior of droplets at superheated conditions on superhydrophilic surfaces due to induced evaporation. The effect of superheat and droplet size are discussed in sections 4.1 and 4.3 respectively while the quasi-steady state non-wetting to wetting transition of droplets is discussed in section 4.2. We will also present experimental data showing the dependence of the observed wetting transition on droplet size.

4.1 Effect of Superheat

Water droplets deposited on a microstructured silicon surface at low superheat wet the surface completely as shown in Fig. 4-1a owing to improved wettability due to roughness. However, these droplets become non-wetting at elevated superheat due to evaporation. This non-wetting behavior is shown in Fig. 4-1b where a droplet sits on top of the structured surface without wetting at 90 °C superheat. The superheat at which the switch in wettability (from a non-wetting to a wetting state) occurs is termed as the critical superheat. This critical superheat was observed to vary based on pillar array geometry (diameter, height, and center-to-center spacing) and also on the size of the droplet.

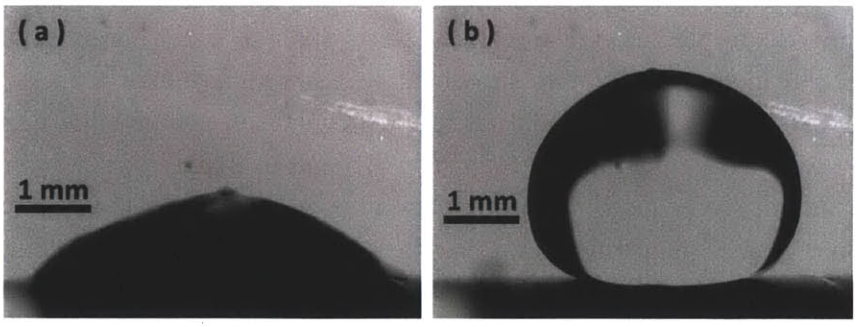

Figure 4-1: (a) Wetting droplet boiling at low superheat (ΔT = 19 °C) (b) non-wetting droplet at elevated superheat (ΔT = 90 °C).

To investigate this behavior further for specific pillar array geometry, we kept the substrate superheat constant and deposited ten droplets using a pipette. The result showed that there are three distinct regions as shown in Fig. 4-2 where the percentage of non-wetting droplets obtained out of ten droplets is shown at each superheat. Figure 4-2 shows that all droplets deposited below 63 °C superheat wetted the surface while non-wetting droplets were obtained 100 % of the time when the superheat was kept above 75 °C. Between 63 °C and 75 °C

superheat, however, a droplet could be in either state (wetting or non-wetting) depending on how gently it was dispensed onto the substrate [33]. Nonetheless, the probability of obtaining a non-wetting droplet monotonically increased as the superheat increased demonstrating a higher chance of obtaining a non-wetting droplet at higher superheats. The result also demonstrates that an inherently superhydrophilic surface at room temperature can behave as superhydrophobic surface due to evaporation-induced non-wetting behavior of droplets. By sufficiently superheating the substrate, enough vapor can be generated to support the droplet from sinking into the microstructured surface and wet.

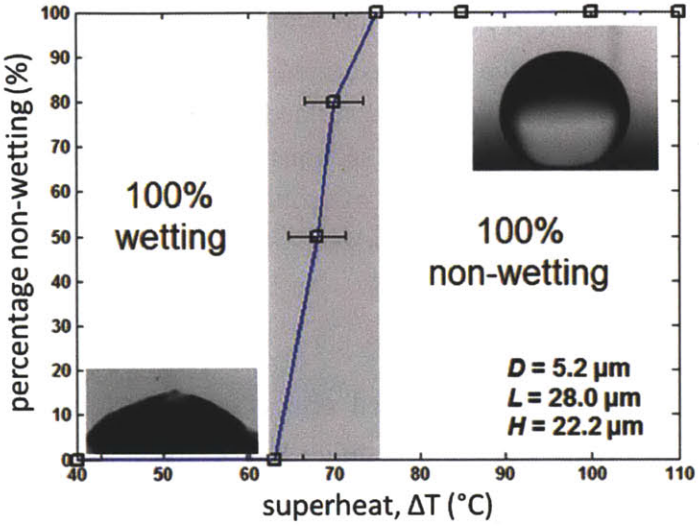

Figure 4-2: Percentage of non-wetting droplets as a function of superheat on a superhydrophilic surface. Both states can reside in the grayed region.

4.2 Quasi-steady State Wetting Transition

To initially deposit a non-wetting droplet, a higher steady state superheat was required to avoid premature wetting of droplets due to transient effects such as water hammer. Once successfully deposited, a second lower steady state superheat was sought to observe the wetting transition. Both superheats are shown in Fig. 4-3b. Droplets on surfaces at high superheat as in the initial deposition stage were very dynamic in nature and difficult to image. For convenient imaging, we used a 25 μm gold wire to position the droplet and keep it in focus for the camera. This gold wire is visible in some of the images in Fig. 4-3a where it was in focus coincidentally. In the other images where it's not shown, it was out of focus. Also, the force exerted by this wire is very small when compared to the other forces involved in the process.

A typical experimental data is shown in Fig. 4-3. Time lapse images of the droplet from which the droplet volume is calculated using a MATLAB script is shown in Figure 4-3a. A plot of droplet volume measured from the acquired images as a function of time is also shown in Fig. 4-3c. The droplet transitions at 35.1 s (Fig. 4-3b) and its volume just before transition was 6.4μL (Fig. 4-3c) while the steady state transition superheat was 26 °C (Fig. 4-3b).

This experimentally observed steady state transition superheat is much lower than the superheat required for Leidenfrost drops on flat surfaces [46]. Moreover, as pointed out by Kim

et al., [47] micro-/nano-porosity delays the Leidenfrost phenomena by initiating heterogeneous bubble nucleation which disrupts the formation of a steady vapor film as required for Leidenfrost drops. Hence, if anything, the Leidenfrost temperature for our test samples (textured surfaces) is expected to be much higher than the Leidenfrost temperature for flat surfaces ~ 260-310 °C [46]. Also, our droplets are sitting on top of the pillar array structure actually touching the tip of the pillars while Leidenfrost drops are completely separated from the heated surface by a continuous vapor cushion.

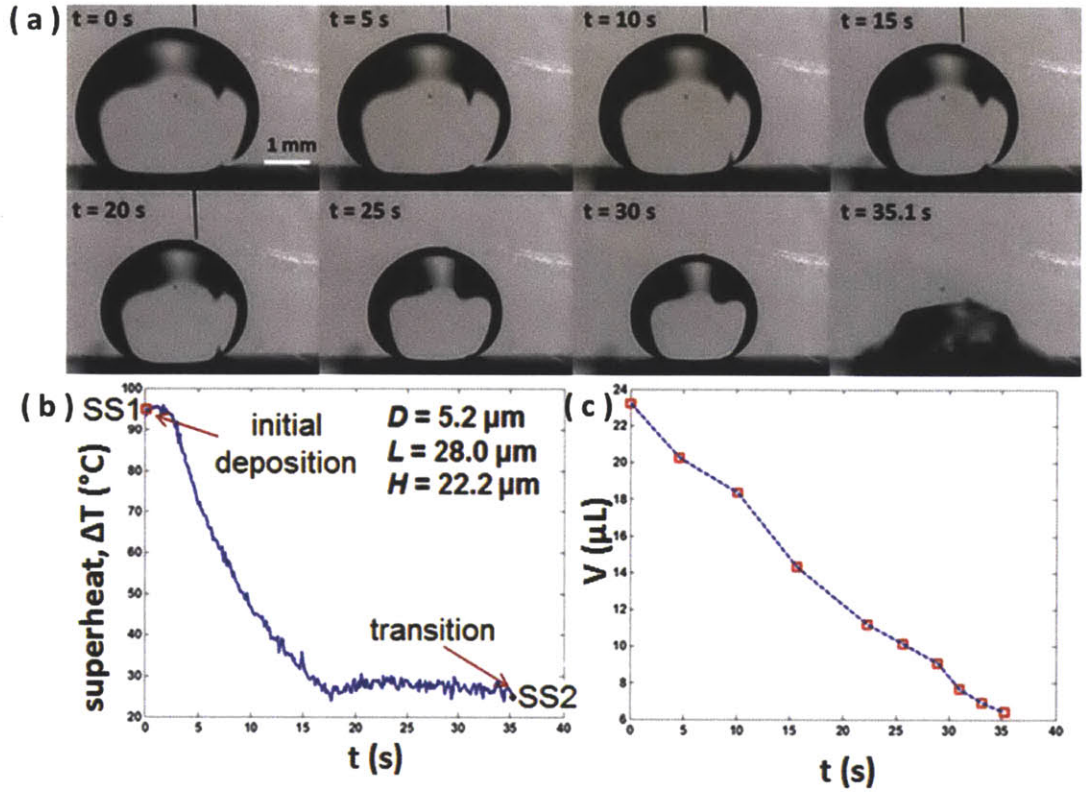

Figure 4-3: (a) Time lapse images of an evaporating droplet at 5 s intervals, (b) corresponding superheat as a function of time, (c) droplet volume as a function of time.

4.3 Effect of Droplet Size

A water droplet is gently deposited on a superhydrophilic surface at a higher superheat. Then the substrate superheat is suddenly decreased to a lower steady state value by toggling a three-way switch (Fig. 3-7). The droplet evaporates at a steady state superheat until it finally transitions to a wetting state. The superheat is measured using a TC and images of the droplet are captured using a high speed camera (Phantom 7.3, Vision Research). The two data are later synchronized to extract the parameters of interest such as transition volume and steady state superheat. The results for five test samples are shown in Fig. 4-4a-e.

The results indicate that the substrate superheat and droplet volume at transition are inversely related, *i.e.* smaller droplets require higher superheat to transition from non-wetting to a wetting state and vice versa. All the samples investigated in this study demonstrated this trend with some scattering of data which we attribute to measurement uncertainty.

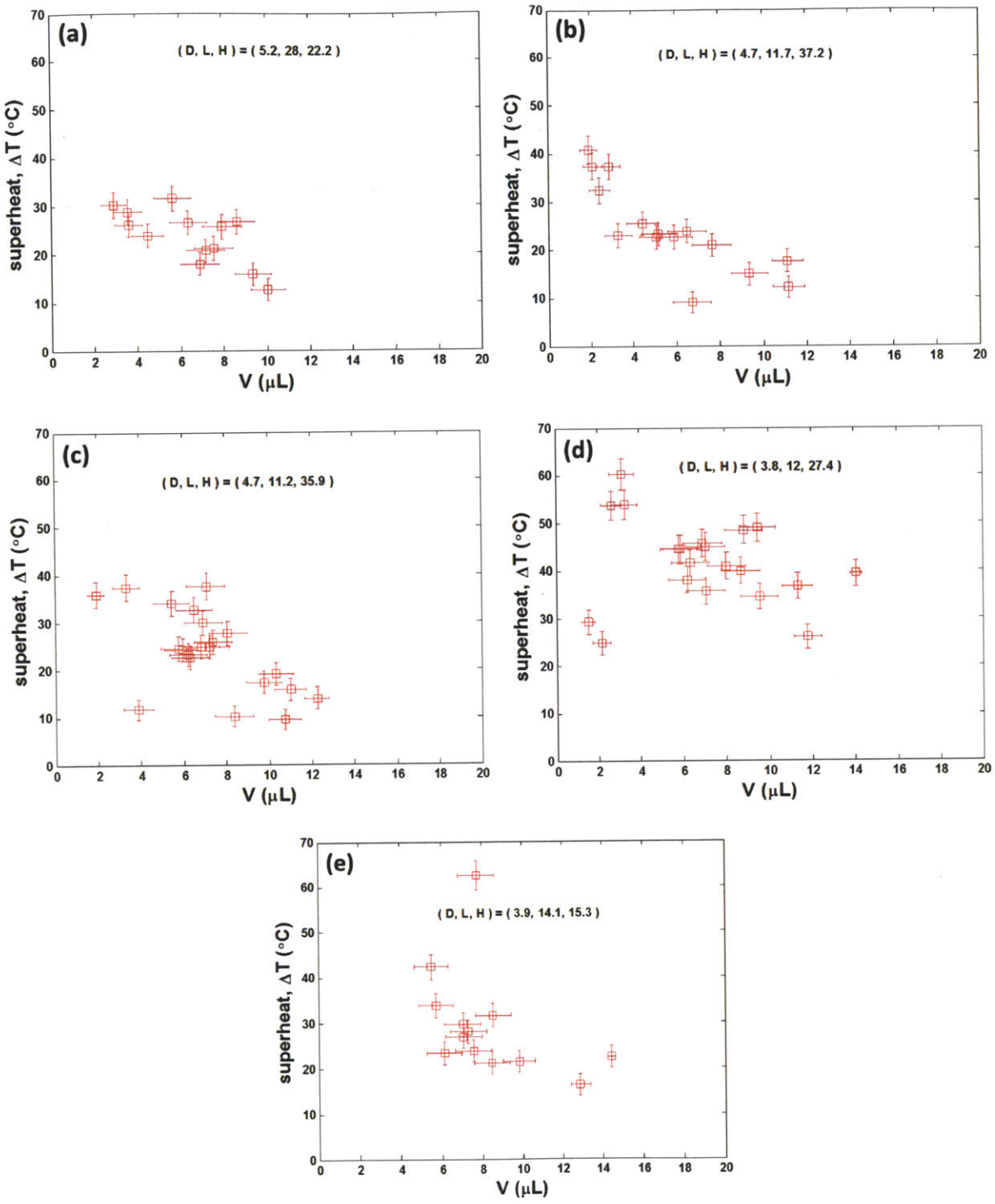

Figure 4-4: Superheat as a function of droplet volume with pillar array geometry of (a) D = 5.2 μm, L= 28.0 μm, H = 22.2 μm, (b) D = 4.7 μm, L= 11.7 μm, H = 37.2 μm, (c) D = 4.7 μm, L= 11.2 μm, H = 35.9 μm, (d) D = 3.8 μm, L= 12.0 μm, H = 27.4 μm, and (e) D = 3.9 μm, L= 14.1 μm, H = 15.3 μm.

4.4 Summary

We have experimentally demonstrated that non-wetting droplets can reside on superhydrophilic surfaces at superheated conditions due to evaporation. We have also shown that the wetting state of a droplet (whether it's wetting or non-wetting) depends on surface superheat. Below a certain critical surface superheat, all droplets wet while no droplet wets the surface above this critical superheat. We also have observed that there exists an overlapping region between the two regions where droplets can be wetting or non-wetting depending on other factors such as deposition technique and drop height. In the overlapping region, the chance of observing a non-wetting droplet increases monotonically with surface superheat.

An inherently superhydrophilic surface at room temperature can take on the characteristics of a superhydrophobic surface due to induced evaporation if the substrate is superheated beyond a critical superheat. This behavior is demonstrated on silicon pillar arrays where droplets can sit on these surfaces without wetting at superheats as low as 26 °C. This phenomenon is distinctively different from Leidenfrost since droplets stay in contact with pillar tops. Moreover, the observed phenomenon is occurring at a much lower temperature than what is reported for Leidenfrost temperature for even flat surfaces [46].

The experimental data shows that the superheat and droplet volume at transition are inversely related to each other *i.e.* smaller droplets require higher superheat to transition from non-wetting to wetting state while bigger droplets require relatively smaller superheat. This is in agreement with experimental observation.

CHAPTER 5

5. Modeling

A droplet sitting on top of a structured surface at superheated conditions evaporates fast enough to induce a pressure force that pushes the droplet upward and hence non-wetting droplets on structured surfaces at superheated conditions. This induced pressure force which prohibits wetting is counteracted by the surface tension force and the weight of the droplet. The force balance between these two competing forces determines whether the droplet will wet or not wet the surface. The simple 1-D model based on force balance explains the transition behavior and follows the general trend observed experimentally. In this chapter, we will develop a model based on a force balance using the basic conservation laws and compare model prediction with experimental data. Using the force balance argument, we will construct a regime map which separates the wetting from the non-wetting regime by an equilibrium transition line.

5.1 Model Formulation

To explain the observed change in the wetting behavior of droplets on structured surfaces at superheated conditions, we developed a simple 1-D lubrication type model which is valid after transient effects such as dynamic and water hammer pressure have dissipated and a steady state condition is established. The phenomenon is modeled as a spherical droplet sitting on top of structured surface at superheated conditions as shown on Fig. 5-1. Due to the improved thermal conductivity of the medium which is composed of silicon pillars and water vapor, the droplet is evaporating faster than a droplet sitting on a vapor cushion. We further assume uniform heat flux at the droplet base, uniform evaporation rate from the base area of the droplet, and 1-D heat conduction through the porous media. We also assume that the evaporation occurs only at the droplet base since the contribution of the evaporation from the surface of the droplet is small compared to the evaporation from the base.

The major radius R_0 and the base radius R of the droplet are related through the Cassie-Baxter relation for composite surfaces. Heat is conducted through the substrate base thickness h and the vapor-pillar porous media of thickness H (which is the same as the pillar height) inducing evaporation at the three phase contact line. As the vapor escapes radially outwards through the vapor-pillar porous media, a pressure gradient is created that supplies the necessary anti-wetting force which is required for suspending the droplet on the pillar top. The droplet is in equilibrium when the sum of all forces which induce wetting is balanced by the pressure force which protects the droplet from sinking down into the pillar array structure and wet.

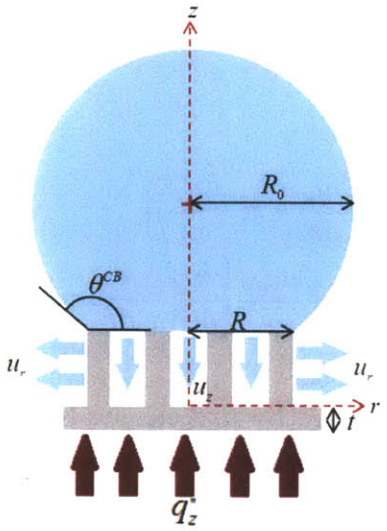

Figure 5-1: Schematic (not to scale) of an evaporating droplet on top of a structured surface.

5.2 Scaling and Conservation Laws

The conservation of mass in polar coordinates is given by,

$$\frac{1}{r}\frac{\partial}{\partial r}(ru_r) + \frac{\partial u_z}{\partial z} = 0, \tag{5-1}$$

where u_r and u_z are the radial and z-direction velocities respectively. The radial velocity scales as the droplet base radius R whereas the z-direction velocity scales as the pillar height H. The scaling for the z-direction velocity becomes,

$$u_z \sim \left(\frac{H}{R}\right) u_r. \tag{5-2}$$

Since $(H/R) << 1$ from geometry, Eq. 5-2 implies that the z-direction velocity is insignificant when compared to the radial velocity. Therefore, the z-direction velocity can be dropped out from the momentum equation.

The momentum equation for porous media is given by [48],

$$\rho_{vap}\left(\frac{1}{\varepsilon}\frac{\partial \underline{u}}{\partial t} + \frac{1}{\varepsilon^2}(\underline{u}.\underline{\nabla})\underline{u}\right) = -\underline{\nabla}p + \frac{\mu_{vap}}{\varepsilon}\nabla^2\underline{u} - \frac{\mu_{vap}}{K}\underline{u}, \tag{5-3}$$

where $\underline{\nabla}p$ is the dynamic pressure gradients, K is the permeability of the vapor-pillar porous media (unit m^2), ε is the porosity (unitless), ρ_{vap} and μ_{vap} are the density and dynamic viscosity of vapor respectively. The dynamic pressures is given by Eq. 5-4,

$$\underline{\nabla} p = \underline{\nabla} P - \rho g. \tag{5-4}$$

The z-component of Eq. 5-3 becomes,

$$\begin{aligned} \rho_{vap} \left\{ \frac{1}{\varepsilon} \frac{\partial u_z}{\partial t} + \frac{1}{\varepsilon^2} \left(u_r \frac{\partial u_z}{\partial r} + u_z \frac{\partial u_z}{\partial z} \right) \right\} \\ = -\frac{\partial p}{\partial z} + \frac{\mu_{vap}}{\varepsilon} \left\{ \frac{\partial}{\partial r} \left(\frac{1}{r} \frac{\partial}{\partial r} (r u_z) \right) + \frac{\partial^2 u_z}{\partial z^2} \right\} - \frac{\mu_{vap}}{K} u_z. \end{aligned} \tag{5-5}$$

Equation 5-5 can further be simplified by making the following assumptions: (a) steady state vapor flow, and (b) the z-component velocity is small compared to the radial component which followed from Eq. 5-2. Hence Eq. 5-5 reduces to,

$$\frac{\partial p}{\partial z} = 0. \tag{5-6}$$

Equation 5-6 implies that the pressure is not a function of the z-direction; it's a function of only the radial direction, hence $p(r, z) = p(r)$. The r-direction momentum equation can be simplified in a similar manner as follows,

$$\begin{aligned} \rho_{vap} \left\{ \frac{1}{\varepsilon} \frac{\partial u_r}{\partial t} + \frac{1}{\varepsilon^2} \left(u_r \frac{\partial u_r}{\partial r} + u_z \frac{\partial u_r}{\partial z} \right) \right\} \\ = -\frac{\partial p}{\partial z} + \frac{\mu_{vap}}{\varepsilon} \left\{ \frac{\partial}{\partial r} \left(\frac{1}{r} \frac{\partial}{\partial r} (r u_r) \right) + \frac{\partial^2 u_r}{\partial z^2} \right\} - \frac{\mu_{vap}}{K} u_r. \end{aligned} \tag{5-7}$$

To retain the dominant terms and drop out the less important ones from the equation, the radial direction momentum equation is non-dimensionalized by scaling the radial velocity with $u_r \sim U$, the radial distance with $r \sim R$ and the z-direction distance with $z \sim H$. Equation 5-7 then simplifies to the non-dimensional momentum equation shown in Eq. 5-8,

$$\begin{aligned} Re_H \left(\frac{H}{R} \right) \left\{ \frac{1}{\varepsilon} \left(\tilde{u}_r \frac{\partial \tilde{u}_r}{\partial \tilde{r}} + \tilde{u}_r \frac{\partial \tilde{u}_r}{\partial \tilde{z}} \right) \right\} \\ = -\frac{\varepsilon H^2}{U R \mu_{vap}} \frac{\partial p}{\partial \tilde{r}} + \left(\frac{H}{R} \right)^2 \frac{\partial}{\partial \tilde{r}} (\tilde{r} \tilde{u}_r) + \frac{\partial^2 \tilde{u}_r}{\partial \tilde{z}^2} - \frac{\varepsilon H^2}{K} \tilde{u}_r. \end{aligned} \tag{5-8}$$

We have shown previously that $(H/R) << 1$ and hence $(H/R)^2 << 1$ follows. The flow is assumed to be laminar and $Re_H(H/R) << 1$. As a result, Eq. 5-8 can be further simplified to,

$$-\frac{\partial p}{\partial r}+\frac{\mu_{vap}}{\varepsilon}\left(\frac{\partial^2 u_r}{\partial z^2}\right)-\frac{\mu_{vap}}{K}u_r=0. \tag{5-9}$$

However, the pressure gradient is shown to be independent of the z-direction in Eq. 5-6, and hence $\partial p/\partial r = dp/dr$. Using this approximation Eq. 5-9 can be rewritten as,

$$\frac{\mu_{vap}}{\varepsilon}\left(\frac{\partial^2 u_r}{\partial z^2}\right)-\frac{\mu_{vap}}{K}u_r-\frac{dp}{dr}=0. \tag{5-10}$$

From which the classical momentum equation for porous media (Brinkman equation) can be obtained by rearranging some of the terms (see Eq. 5-22)

5.3 Mathematical Formulation

The droplet base which is in contact with the pillar top is assumed to be at saturation temperature at 1 atm. (100 °C). Uniform evaporation rate at the droplet base is assumed. The droplet is sitting on a composite surface which is made from silicon pillars and water vapor. Hence, the apparent contact angle of the droplet was estimated using the Cassie-Baxter equation for composite surfaces [32, 49] as given by Eq. 5-11

$$\cos\,\theta^{CB} = -1+\phi_s(1+r\cos\,\theta_Y). \tag{5-11}$$

Here, ϕ_s is the solid fraction (also called area fraction), and θ_Y and θ^{CB} are the intrinsic contact angle on a chemically homogeneous flat surface and the apparent Cassie-Baxter contact angle on the composite surface, respectively. For a surface with regular texture as shown in the schematic in Fig. 5-2, solid fraction ϕ_s and surface roughness r are given by Eqs. 12 and 13 respectively.

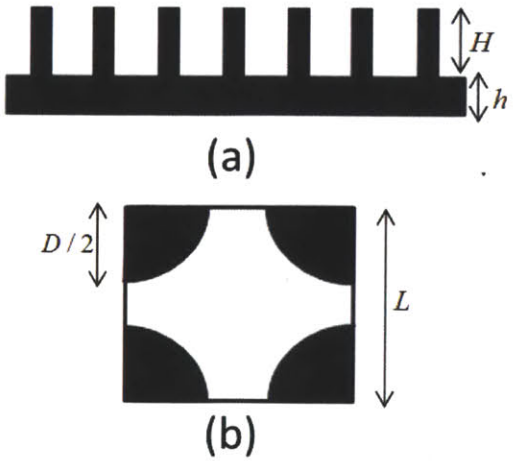

Figure 5-2: Schematic (not to scale) of (a) side and (b) top view of a structured surface showing the pillar diameter *D*, height *H*, center-to-center spacing *L*, and test sample thickness *h*.

$$\phi_s = \frac{\pi D^2}{4L^2}, \tag{5-12}$$

$$r = 1 + \frac{\pi DH}{L^2}, \tag{5-13}$$

where D, L, and H are the pillar diameter, center-to-center spacing and height as shown by the schematic in Fig. 5-2. The solid fraction of our test samples vary from 0.03 to 0.14.

The test samples we investigated for this study meet the imbibition condition which is given by Eq. 5-14 [24, 30]

$$\cos\theta_{imb} = \frac{1 - \phi_s}{r - \phi_s}, \tag{5-14}$$

where θ_{imb} is the imbibition angle. The imbibition angle is the critical angle below which the droplet spreads to fill the void between pillars following the surface asperities. The discussions that follow and the results shown in this and the next section refer to a sample with pillar diameter, height and center-to-center spacing of 5.2, 28.0, and 22.2 μm respectively. However, the results and conclusions hold true for other samples too.

The Young angle for smooth silicon surface is θ_{si} = 38° and the imbibition angle as per Eq. 5-14 for the test sample under discussion (D = 5.2, H = 28.0, and L = 22.2 μm) is 47° (> 38°) suggesting that a droplet should spread upon touching the structured surface and wet. That was indeed the case observed for experiments carried out at room temperature. The apparent contact angle for the test sample was calculated using the Cassie-Baxter relation given in Eq. 5-11, and it was found to be θ^{CB} = 162° for an intrinsic contact angle of 38° and a solid fraction of 0.03. This calculated apparent contact angle is different from the experimentally measured apparent contact angle of θ_{app} = 149° ± 2° (Fig. 3-6). The difference between the experimental and the predicted values of the apparent contact angle can be attributed to measurement uncertainties in the experiment and the fact that the Cassie-Baxter relation is valid for sessile droplets only. However, the current study investigates an evaporating droplet and hence a receding contact angle would be the more appropriate choice. Based on the apparent contact angle defined by Eq. 5-11, a relation between the droplet base radius R and major radius R_o can be established from geometry by assuming a spherical droplet as,

$$R = R_0 \sin\theta^{CB}. \tag{5-15}$$

The effect of gravity on the shape of the droplet is ignored in the analysis since the dimensionless Bond number at transition was found to be less than unity for all experiments (Bo is approximately 0.2, for the particular case discussed in Fig. 4-3 where the droplet transitioned at 6.4 μL which corresponds to a major radius of 1.2 mm),

$$Bo = \frac{g(\rho_{liq} - \rho_{vap})R_0^2}{\gamma_{LV}}, \tag{5-16}$$

where g is acceleration due to gravity (g = 9.81 m/s^2), ρ_{liq} and ρ_{vap} are the density of liquid and vapor respectively, and γ_{LV} is the surface tension at the liquid-vapor interface. Also, the capillary length shown in Eq. 5-17 (denoted a, unit m) for the droplets was found to be less than the capillary length of water (2.7 mm),

$$a = \sqrt{\frac{\gamma_{LV}}{\rho_{liq} g}}. \tag{5-17}$$

We further assume that the heat conducted through the porous media is completely utilized to induce uniform evaporation at the liquid-vapor interface of the droplet base area. The vapor escapes from the droplet base with velocity $\bar{u}_z$ in the z-direction and could be related to the assumed 1-D heat conduction through the composite media as

$$\bar{u}_z = -\frac{k_{eff}\Delta T_p}{H\rho_{vap}h_{fg}}, \tag{5-18}$$

where ρ_{vap} and h_{fg} are the density of vapor and the latent heat of vaporization respectively, ΔT_p is the temperature difference between the pillar top and the pillar base, and k_{eff} is the effective thermal conductivity of the porous media which is composed of the silicon pillars and the water vapor which is estimated by Eq. 5-19 from [50]

$$k_{eff} = (1 - \phi_s)k_{vap} + \phi_s k_{si}. \tag{5-19}$$

Notice that the thermal conductivity of the porous media is orders of magnitude higher than the thermal conductivity of water vapor for all the samples investigated in this work. This is not surprising given the high thermal conductivity of silicon compared to the thermal conductivity of water vapor. Considering that (H/R) << 1, it is assumed that the z-direction velocity u_z is small compared to the radial direction vapor velocity u_r (*i.e.*, u_z/u_r << 1, here u_z is constant because of the previous assumption of uniform evaporation). The continuity equation at any radial position under the droplet base radius r can then be written as

$$\int_0^H u_r(r,z)\,(2\pi r)dz = \pi r^2 \bar{u}_z. \tag{5-20}$$

Equations 5-18 and 5-20 can be combined to obtain a relation between the radial velocity and temperature difference between the pillar base and pillar top as

$$\frac{1}{H}\int_0^H u_r(r,z)\,dz = -\left(\frac{k_{eff}\Delta T_p}{2\rho_{vap}h_{fg}}\right)\frac{r}{H^2}. \tag{5-21}$$

Since (H/R) << 1, further assumptions can be made that simplify the analysis as follows: (1) the viscous loss is dominated by the velocity gradient in the z-direction *i.e.*, the radial velocity is a function of z-direction only, $u_r(z)$, (2) momentum changes in the axial direction can be neglected, only the z-component momentum change is important, and (3) the pressure depends only in the radial direction, $\partial p/\partial z = 0$ (Eq. 5-6). Using these assumptions, the classical momentum equation for porous media can be simplified to obtain the Brinkman equation,

$$\frac{\partial^2 u_r}{\partial z^2} - \frac{\varepsilon}{K}u_r = \frac{\varepsilon}{\mu_{vap}}\frac{dp}{dr}, \tag{5-22}$$

where $\varepsilon = 1 - \pi D^2/4L^2$ is the dimensionless porosity, μ_{vap} is absolute viscosity of saturated vapor, and K is the permeability of the porous media. The permeability was calculated using an asymptotic expression which is valid for flows through dilute pillar arrays, $\phi_s \leq 0.25$ [51]. Equation 5-22 is then solved by applying the no-slip boundary conditions at the pillar base and pillar top. The velocity profile is a function of both the radial and vertical direction $u_r(r,z)$ as given by Eq. 5-23

$$u_r(r,z) = \frac{K}{\mu_{vap}}\left(\frac{dP}{dr}\right)\left(\frac{e^{-\beta z}(-1+e^{\beta z})(-e^{\beta z}+e^{\beta z})}{1+e^{\beta z}}\right), \tag{5-23}$$

where $\beta = \sqrt{\varepsilon/K}$ (unit m^{-1}). The vapor velocity is zero at the center of the base area of the droplet and it increases radially outwards reaching a maximum at the exit. The maximum velocity profile at the exit (r=R) is shown in Fig. 5-3 (D = 5.2 μm, L= 28.0 μm, H = 22.2 μm, V= 12 μL, and superheat ΔT = 30 °C). Droplet volume and superheat are selected to represent typical experimental values obtained from observation.

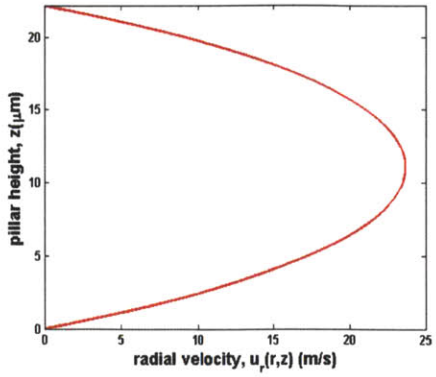

Figure 5-3: Typical velocity profile of vapor flowing through a vapor-pillar porous media.

An average radial velocity which depends only in the radial direction can then be obtained by integrating the two dimensional velocity profile $u_r(r, z)$ in the vertical direction from the pillar base to the pillar top. This average radial velocity is given by Eq. 5-24 and is shown in Fig. 5-4 along with the Reynolds number based on the hydraulics diameter $D_h=4A_c/p$ (A_c is the cross sectional area of the vapor flow and p is the wetted perimeter) which in this case is twice the pillar height ($D_h=2H$). The Reynolds number is small suggesting that the vapor flow is indeed laminar which agrees with the previous assumption made to simplify the momentum equation.

$$\bar{u}_r(r) = \frac{K}{\mu_{vap}}\left(\frac{dP}{dr}\right)\left(-1 + \frac{2\tanh\left(\frac{1}{2}H\beta\right)}{H\beta}\right), \tag{5-24}$$

$$Re_{D_h} = \frac{\rho_{vap}\bar{u}_r D_h}{\mu_{vap}}. \tag{5-25}$$

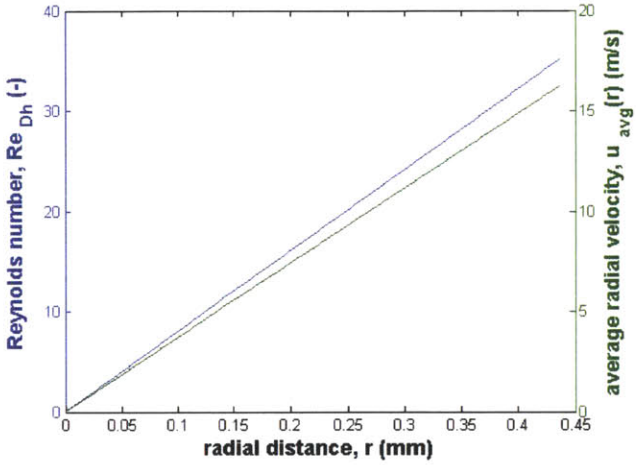

Figure 5-4: Typical average radial velocity of vapor flowing through a vapor-pillar porous media (V= 12 µL, ΔT = 30 °C). The radial velocity is computed at the exit where the average radial velocity and the Reynolds number are maximum.

The average radial velocity from Eq. 5-24 is then equated with the average velocity obtained from Eq. 5-21 (which is obtained by integrating the 2-D velocity profile) assuming 1-D heat conduction to obtain the pressure profile along the radial direction as

$$P(r) - P_{amb} = -\left(\frac{\mu_{vap}k_{eff}\Delta T_p}{4KH^2\rho_{vap}h_{fg}}\right)\left(-1 + \frac{2\tanh\left(\frac{1}{2}H\beta\right)}{H\beta}\right)^{-1}(R^2 - r^2), \tag{5-26}$$

where P_{amb} is the ambient pressure (1 atm.), $P(r)$ is the absolute pressure at a radial distance r from the center of the droplet base. The pressure profile is parabolic with the maximum at the

center of the droplet base and decreasing sharply to ambient pressure at the exit as depicted in Fig. 5-5. This pressure gradient is responsible to provide the necessary force to counterbalance the weight and surface tension forces which act to induce wetting. Notice that the vertical axes is the gage pressure (above ambient) in units of atmosphere.

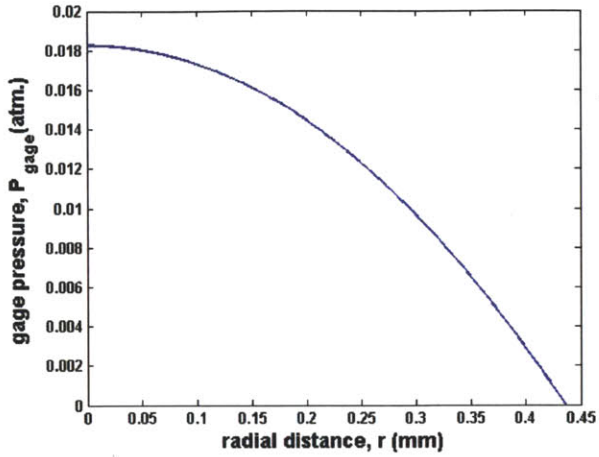

Figure 5-5: Pressure profile underneath an evaporating droplet sitting on a vapor-pillar porous media (V = 12 µL, ΔT = 30 °C).

The upward anti-wetting force on the droplet $F_{anti\text{-}wetting}$ was calculated by integrating the gage pressure obtained in Eq. 5-26 over the droplet base area from $r = 0$ to $r = R$,

$$F_{anti-wetting} = \frac{-\pi\varepsilon\mu_{vap}k_{eff}\Delta T_p}{8KH^2\rho_{vap}h_{fg}}\left(-1+\frac{2\tanh\left(\frac{1}{2}H\beta\right)}{H\beta}\right)^{-1}R^4. \quad (5\text{-}27)$$

As can be seen from Eq. 5-27, the upward force which resists the droplet from wetting the substrate is dependent on fluid properties (which in turn depend on the temperature and pressure of the droplet), the geometry of the pillar array structure including the porosity and permeability, the effective thermal conductivity of the vapor-pillar porous media, and the droplet base radius. The strong dependence on droplet base radius ($F_{anti-wetting} \propto R^4$) is important in explaining the experimental results later.

After dynamic and water hammer pressures have dissipated and steady state conditions prevailed, the downward wetting force on the droplet F_{down} which is comprised of the weight of the droplet and the force due to surface tension is given by

$$F_{wetting} = \rho_{liq}Vg + N\pi D\gamma_{LV}\cos\theta_Y, \quad (5\text{-}28)$$

where V is the droplet volume, ρ_{liq} is the density of liquid water at saturation temperature and pressure, D is the pillar diameter, and $N = \pi R^2/L^2$ is the number of pillars that are in contact with the droplet base. The surface tension force (the second term in Eq. 5-28) scales as $\propto R^2$ (the R^2

term comes from the number of pillars), whereas the weight of the droplet (the first term in Eq. 5-28) scales as $\propto R^3$. The relative magnitude of these two wetting forces and the ratio between them is shown in Fig. 5-6 where it's shown that the major contributor to the downward wetting force is the surface tension. The dominance of the surface tension over the droplet weight is even more pronounced at smaller volumes as shown in Fig. 5-6b. For this reason, we can scale the wetting force to scale as R^2 instead or R^3 ($F_{wetting} \propto R^2$). Previously, we have shown that the anti-wetting force scales as R^4 and hence the anti-wetting force depends more on droplet size than the wetting force. Notice also that the droplet is contacting the substrate locally at the intrinsic contact angle θ_Y as demonstrated by Eq. 5-28.

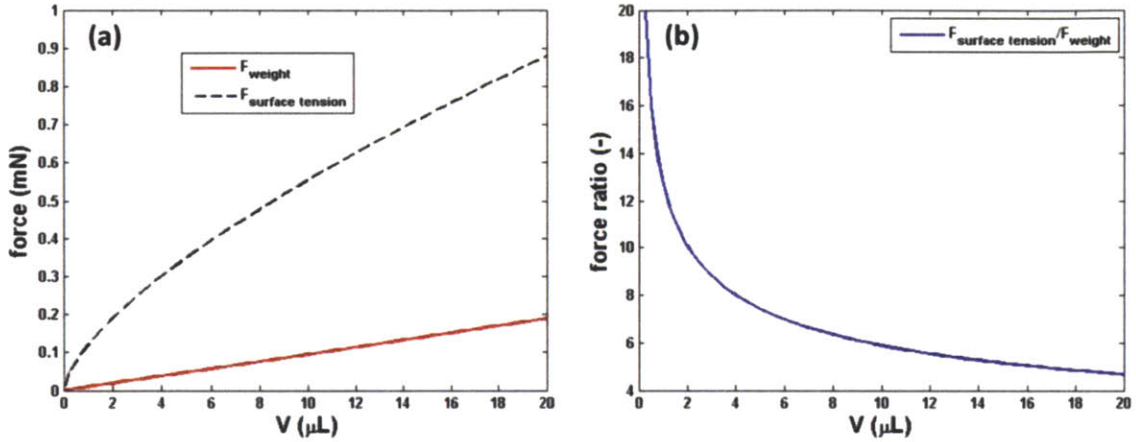

Figure 5-6: Comparison between the droplet weight and the force due to surface tension for 30 ˚C superheat (a) actual magnitudes, (b) relative magnitude (ratio).

The effect of the gold wire which was used to position the droplet for ease of imaging is not considered in the force balance since its magnitude is significantly smaller than the other forces involved in this steady state transition process. The magnitude of the force exerted by the gold wire in comparison with the weight of the droplet and the force due to surface tension is shown in Fig. 5-7 which indeed verifies the claim. The force due to the gold wire is given by Eq. 5-29 as

$$F_{gold\,wire} = \pi d \gamma_{LV} \cos\theta, \tag{5-29}$$

where γ_{LV} is the liquid-vapor surface tension, d is the diameter of the gold wire which is 25 μm, and θ is the contact angle between the gold wire and the droplet (in this case 0° is used which maximizes the force exerted by the gold wire for worst case scenario, a conservative estimate).

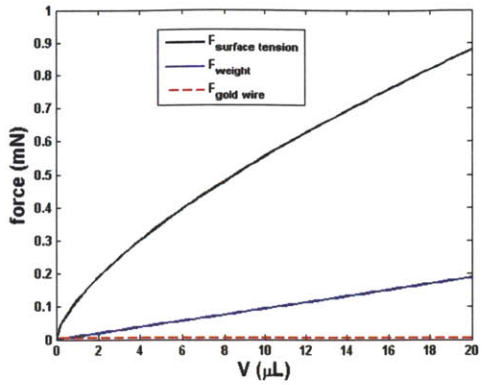

Figure 5-7: Relative magnitudes of the weight of the droplet, the force due to surface tension, and the force exerted by the gold wire.

5.4 Wetting and Non-wetting Regimes

In the previous section, we have shown that the anti-wetting force comes from the pressure gradient whereas the wetting force comes from the weight of the droplet and the force due to surface tension. Moreover, we have shown how the two competing forces scale. The anti-wetting force scales as R^4 whereas the wetting force scales as R^2 where R is the radius of the droplet. Because of this unequal scaling, the wetting force decreases slower than the anti-wetting force as the droplet evaporates which is in agreement with experimental observation.

A typical experiment starts at a higher volume (to compensate for the evaporation that takes place before reaching steady state) and a higher superheat (to overcome the transient effects such as water hammer pressure and avoid premature wetting transition). When depositing the droplet initially at the start of the experiment, the anti-wetting force is predominantly bigger in magnitude than the wetting force and hence non-wetting droplets. However, as the droplet evaporates the magnitude of the anti-wetting force decreases faster than the wetting force (remember that the anti-wetting force scales as R^4 and hence it starts bigger and dies faster). The magnitudes of these two forces as the droplet is evaporating (moving from right to left on the x-axis in the direction of decreasing droplet volume) are shown in Fig. 5-8. The two forces cross each other at a particular point that defines an equilibrium point where the two forces are equal in magnitude but opposite in direction. As the droplet continues to evaporate (moving further to the left), this force balance is disturbed and the droplet is not in equilibrium anymore. Note that Fig. 5-8 is produced for specific pillar geometry at a unique superheat (40 °C in this case). Changing either the superheat or the pillar array geometry will result in a different plot with a similar trend. The volume where the two forces cross each other is called a transition volume. Before reaching the transition volume, the non-wetting force is bigger than the wetting force and hence the droplet is non-wetting. Likewise, droplets smaller than the transition volume are wetting since wetting forces dominate over the non-wetting force in this regime.

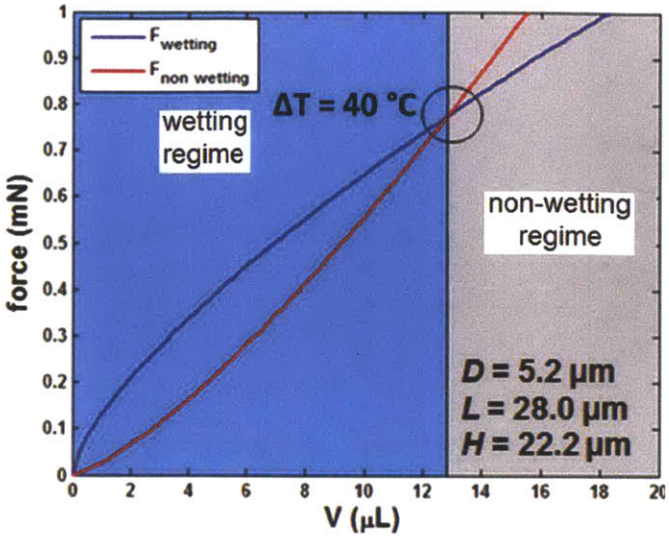

Figure 5-8: A plot delineating the wetting and non-wetting regimes for a 40 °C superheat.

The superheat that is required to balance the two competing forces is obtained by equating the wetting and anti-wetting forces and solve for the superheat,

$$\Delta T_p = \frac{\rho_{liq} V g + N\pi D \gamma_{LV} \cos\theta_Y}{\frac{-\pi\varepsilon\mu_{vap}k_{eff}}{8KH^2\rho_{vap}h_{fg}}\left(-1+\frac{2\tanh\left(\frac{1}{2}H\beta\right)}{H\beta}\right)^{-1} R^4}. \tag{5-30}$$

Equation 5-30 estimates the temperature difference between the pillar base and pillar top (ΔT_p) that is required to sustain a non-wetting droplet on top of the pillar array structure in a quasi steady state condition. An additional temperature drop between the pillar base and the backside of the substrate is required to match the experimentally measured wall temperature with the model prediction. Incorporating this additional temperature drop across the thickness of the test sample and assuming 1-D heat conduction, the overall temperature drop from the backside of the test sample to the pillar top (ΔT) can be computed as,

$$\Delta T = \Delta T_p \left(1 + \frac{H k_{eff}}{h k_{Si}}\right). \tag{5-31}$$

The contribution of the thickness of the test sample (ΔT_{sub}) and the vapor-pillar porous media (ΔT_p) to the overall superheat (ΔT) is shown in Fig. 5-9.

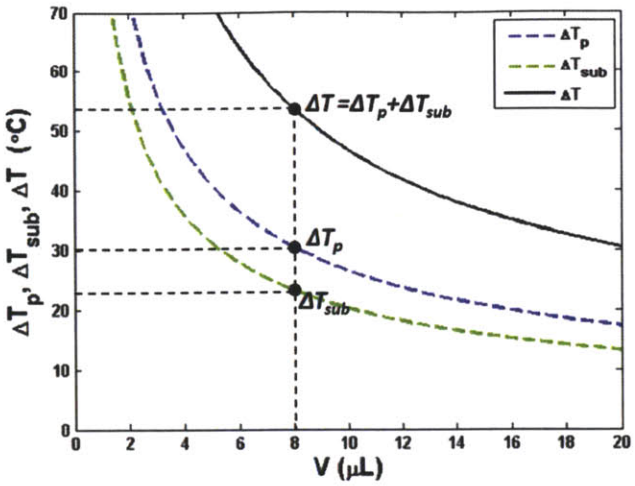

Figure 5-9: Contributions of sample thickness and vapor-pillar porous media to the overall superheat.

The anti-wetting force depends on the evaporation rate and hence on surface superheat. On the other hand, we speculate that the wetting force is insensitive to superheat. For this reason, only the non-wetting force (dashed line, Fig. 5-10) responds to changes in superheat while the solid blue line remains the same (Fig. 5-10). Hence, we can obtain locus of equilibrium points by varying the superheat and locating where the two lines cross each other. This method will produce locus of points defined by superheat and transition volume where the two forces are in perfect balance. The line of equilibrium points so produced is called transition line.

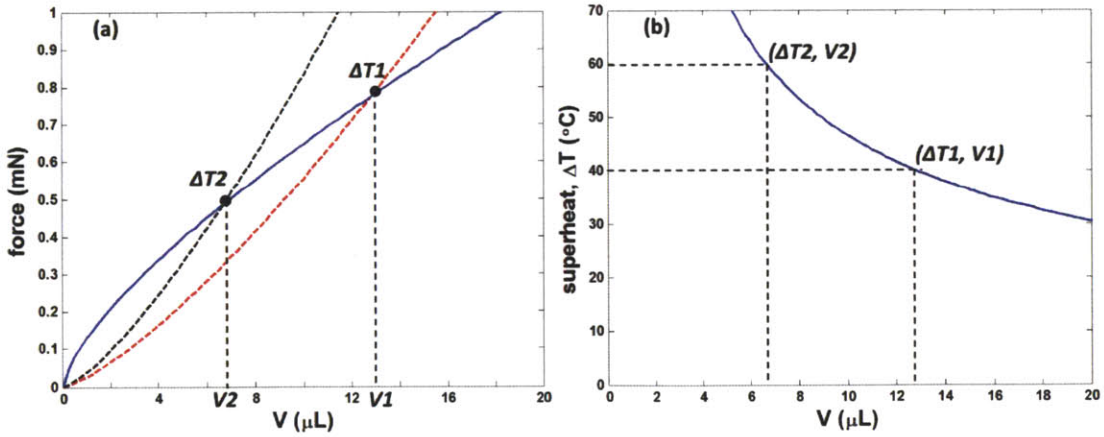

Figure 5-10: Generating locus of equilibrium points.

Figure 5-10b defines the equilibrium line which delineates the wetting from the non-wetting regime. As pointed out earlier, this plot is dependent on pillar array geometry. A different geometry will give a different plot with a similar trend. Either way, the trend shows that smaller droplets require higher superheat to transition from a non-wetting to a wetting state and vice versa. By producing such plots for a specific pillar array geometry, one can determine whether a droplet would wet or not wet the surface given the droplet volume and the surface superheat. Remember that due to the initial requirement of higher temperature and bigger droplet

volume, experiments have to commence from the top right corner and transition occurs as the droplet volume decreases from right to left on the graph at constant superheat.

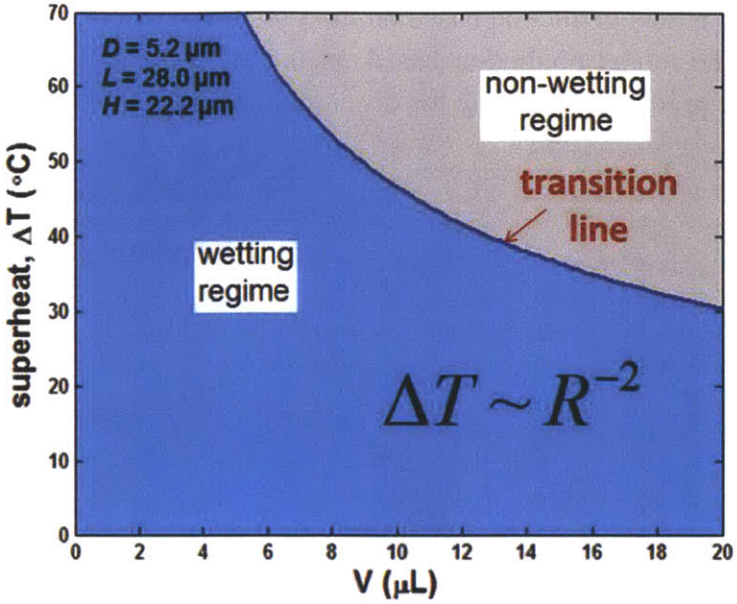

Figure 5-11: Wetting and non-wetting regimes separated by a transition line.

The wetting regime in Fig. 5-11 is favored by small diameter, sparse and tall pillars. This combination shifts the transition line upward increasing the wetting regime. This is shown in Fig. 5-12 where downward and upward arrows indicate decrease and increase in the indicated parameter. The dimensions shown in the legend are all in µm. Notice how much the blue line shifted upward for only small changes in the pillar geometry. This result demonstrates how sensitive the observed phenomenon is to pillar array geometry.

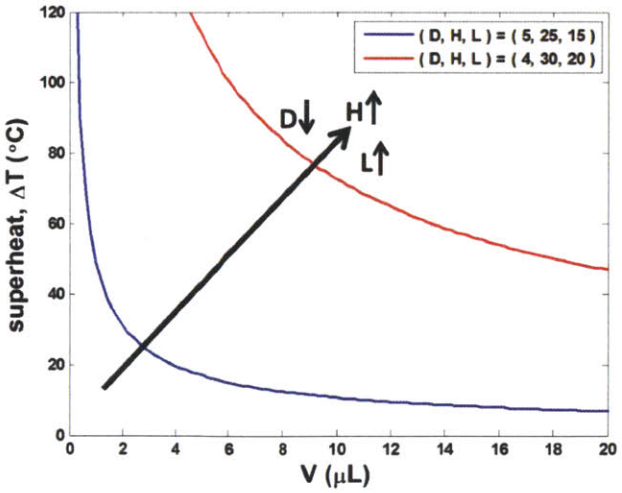

Figure 5-12: Effect of pillar diameter, height and center-to-center spacing on transition line.

5.5 Discussion

The experimentally measured superheats and the model prediction are shown in Fig. 5-13. The solid black line is the model prediction based on the Cassie-Baxter contact angle (162°) while the dotted blue line is the model prediction based on the experimentally measured contact angle (147°). Error bars are produced following the discussion in section 3.4.

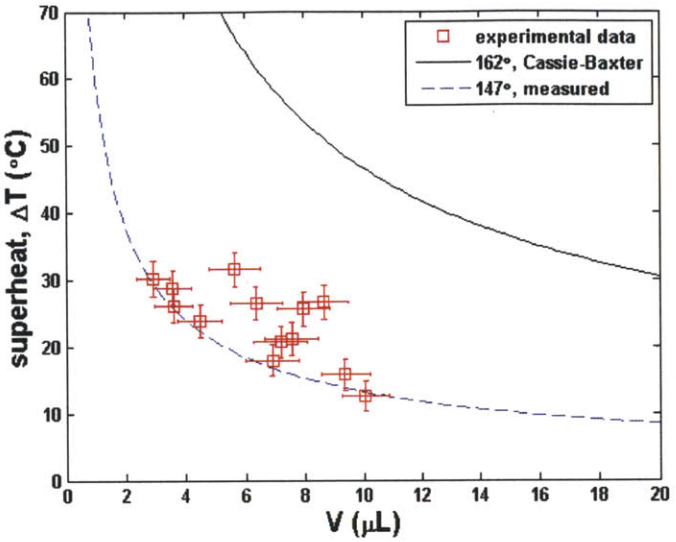

Figure 5-13: Superheat as a function of volume for a droplet deposited on a structured surface (D = 5.2 μm, L= 28.0 μm, and H = 22.2 μm).

Figure 5-13 shows the general trend of increasing transition superheat as the droplet volume decreases which agrees well with experimental observation. It also shows how sensitive the model is to apparent contact angle (ACA). This is so because the base radius is calculated from the major radius using the ACA and that wetting and non- wetting forces depend on the base radius to the power of 2 and 4 respectively. Therefore, small error in predicting the ACA would propagate to the forces and the effect is stronger. That is the reason why the two transition lines in Fig. 5-13 are far apart from each other for small change in the ACA. This indicates that a more accurate prediction of the ACA is necessary to properly match the experimental data with the model prediction.

In the model, the ACA is calculated using the CB relation which is derived for a sessile droplet at room temperature on a composite surface. However, the droplet we are investigating in this study is evaporating, and hence the more appropriate CA would be the receding contact angle instead of the equilibrium Cassie-Baxter contact angle. However, measuring the receding CA of an evaporating droplet on a structured surface is a thesis topic by its own right and is not dealt in this investigation. However, preliminary studies confirm that the ACA of the evaporating droplet is changing with time. This result is shown in Fig. 5-14b where it's shown that the ACA is increasing as the droplet decreases in volume.

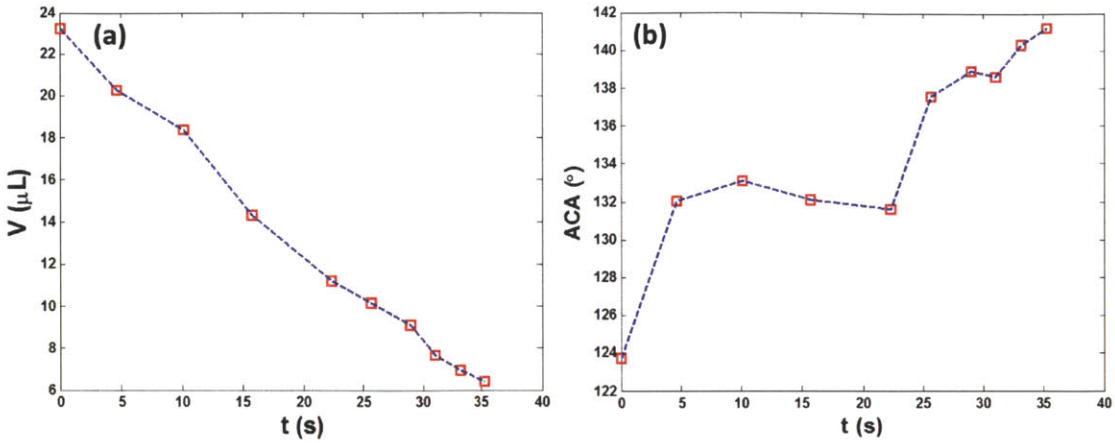

Figure 5-14: (a) Volume as a function of time, (b) ACA as a function of time of an evaporating droplet on a structured surface.

A similar trend as in Fig. 5-13 was observed for other test samples with different pillar array geometry. Four more experimental results are presented in Fig. 5-15. The model prediction that uses the measured CA from the captured images fits the data better (blue broken line) than the CB angle (black solid line) for most samples. All samples investigated in this thesis work show a similar trend of a decreasing superheat with increasing droplet volume. Even though some scattering (which is speculated to come from measurement uncertainty) is observed in some of the test samples, the developed 1-D model predicts the general trend of the inverse relation between droplet volume and surface superheat.

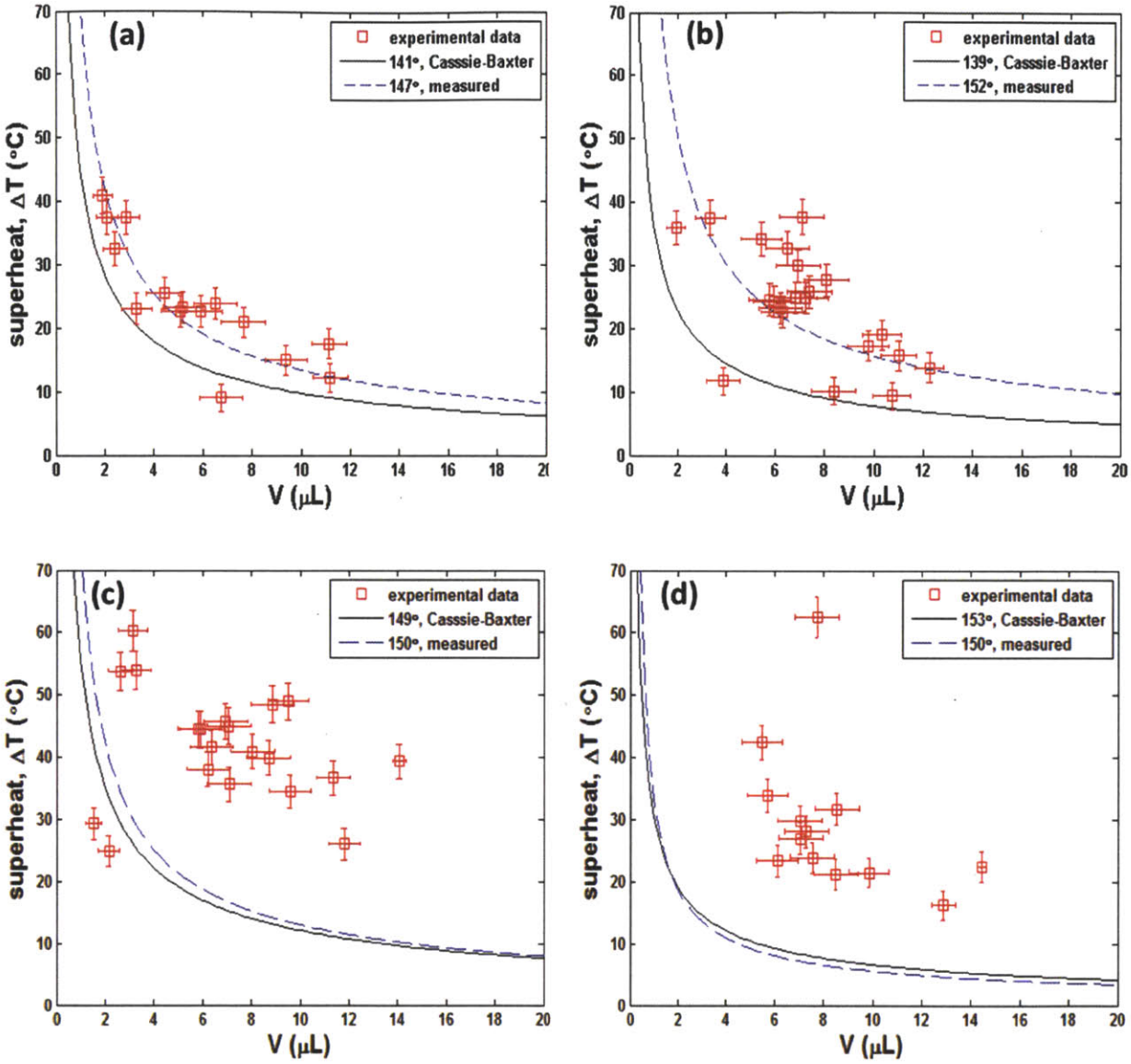

Figure 5-15: Superheat as a function of transition volume (a) D = 4.7 μm, L= 11.7 μm, H = 37.2 μm, (b) D = 4.7 μm, L= 11.2 μm, H = 35.9 μm, (c) D = 3.8 μm, L= 12.0 μm, H = 27.4 μm, and (d) D = 3.9 μm, L= 14.1 μm, H = 15.3 μm.

5.6 Summary

Evaporation-induced wetting transition of water droplets on superhydrophilic microstructured surfaces at superheated conditions has been investigated. We have developed a 1-D lubrication type model based on a force balance to explain the phenomenon. The force balance between two competing forces (wetting and anti-wetting forces) determines whether a droplet will wet or not wet the substrate.

The anti-wetting force originates from the pressure gradient that develops underneath the droplet due to the flow resistance that the vapor encounters as it escapes radially outwards. On the other hand, the wetting force comes from the weight of the droplet and the force due to

surface tension. The force due to surface tension is shown to be the bigger contributor of the wetting force. We speculate that the droplet is in mechanical equilibrium when the two forces are in balance.

Using a scaling argument, we have shown that the anti-wetting force scales to the fourth power while the wetting force scales only to the second power of the droplet radius suggesting that the anti-wetting force depends more strongly on droplet size than the wetting force. Due to this, the anti-wetting force decreases faster than the wetting force as the droplet evaporates. Also, the two competing forces are derived analytically using the basic conservation laws.

We have shown that there are two distinct regimes (wetting and non-wetting) separated by a transition line. The transition line is a locus of equilibrium points where the two competing forces are in perfect balance. Above the transition line is a non-wetting regime and below it is the wetting regime. The droplet transitions from a non-wetting to a wetting state as it crosses the transition line while evaporating at quasi-steady state conditions.

We have also shown that the overall superheat that is required to suspend a droplet comes from two sources: the superheat across the thickness of the test sample and through the vapor-pillar porous media. The contribution of each source is comparable to one another.

Lastly, we speculate that it's the presence of a vapor-pillar porous media that made this phenomenon possible at such low superheats (as low as 26 °C, see Fig. 3-8). Evaporation at the droplet base was enhanced due to increased thermal conductivity because of the presence of silicon pillars. The effective thermal conductivity of the vapor-pillar porous media is orders of magnitude higher than the thermal conductivity of vapor alone. Moreover, the porous nature of the media underneath the droplet (vapor-pillar porous media) resulted in a significant pressure drop as the vapor escapes radially outwards. This flow resistance resulted in a force that counteracts the wetting force on the droplet and hence a suspended droplet sitting on pillar tops.

The developed 1-D lubrication type model predicts an increasing superheat with decreasing droplet volume which is consistent with experimental observation. The analytical expression so obtained showed strong dependence of the observed phenomenon with droplet volume. Overall, the 1-D model captures the trend and more detailed analysis is required to match the experimental data and the model prediction better.

CHAPTER 6

6. Summary and Future Work

In this thesis, we have investigated the wetting transition of droplets on superhydrophilic surfaces at superheated conditions. We have experimentally demonstrated the quasi-steady state transition of droplets from non-wetting to wetting state and showed the relationship between droplet volume and transition superheat. The developed 1-D lubrication type model showed the general trend of decreasing droplet volume with superheat which is consistent with experimental observation. However, the current model is a very simplified model and hence it requires a thorough analysis of the thermal resistance network and revision as new understanding of the process is gained.

6.1 Contribution

The objective of this work is to investigate the wetting behavior of droplet on structured surfaces at superheated conditions. To this end, we believe that the following are the contributions of this thesis work:

(a) Droplets spontaneously spread and wet a superhydrophilic surface upon touching the solid substrate at room temperature. However, we have observed that the same droplets do not wet the surface when the surface is heated beyond a critical superheat. When the substrate is heated above this critical superheat, liquid propagation on the surface ceases and non-wetting droplets form on the surface. Hence, superheat is a factor that determines the wetting state of droplets on structured surfaces. We have also showed that there is a window of superheat (Fig. 4-2) where one can observe both wetting and non-wetting droplets. Above this window region all droplets are non-wetting whereas 100% of the droplets were wetting below this window region.

(b) We have experimentally demonstrated that non-wetting droplets can reside on superhydrophilic surfaces at superheated conditions due to evaporation. This phenomenon is observed at superheats as low as 26 °C due to the enhanced thermal conductivity. Since the thermal conductivity is orders of magnitude higher than the thermal conductivity of water vapor alone, smaller superheat is required to produce enough vapor to protect the droplet from wetting the surface. The escaping vapor encounters resistance from the vapor-pillar porous media which results in a pressure gradient which is responsible for providing the anti-wetting force. The wetting force, on the other hand, is provided by the weight of the droplet and the force due to surface tension. The wetting and anti-wetting forces scale as the second and fourth powers of the droplet base radius and the balance between these two forces determine whether the droplet will wet the heated structured surface or not.

(c) We have also shown that there are two distinct wetting regimes (wetting and non-wetting) which are separated by a locus of equilibrium points called transition line. An evaporating droplet will change its wetting state from a non-wetting to a wetting state as it crosses this

equilibrium line while traversing horizontally from left to right at constant superheat (Fig. 5-11).

(d) The observed phenomenon is dependent on pillar array geometry (pillar diameter, height, and center-to-center spacing). Changing the pillar array geometry will result in a different plot but a similar trend.

(e) We have also showed that the wetting transition of droplets depends on the volume and surface superheat.

(f) We have developed a 1-D lubrication type model that predicts the general trend reasonably well. The model is also shown to be very sensitive to the apparent contact angle.

6.2 Recommendations for Future Work

The work reported in this thesis gives fundamental understanding of the wetting dynamics of droplets on structured surfaces at superheated conditions. It identified the different wetting regimes which depend on pillar array geometry, surface superheat and droplet size. Based on the initial results and the understanding gained through experimental investigation, we propose the following recommendations for future work:

(a) The model we developed assumes 1-D heat conduction. It captures the general trend, but it requires a more thorough analysis of the thermal path to obtain a better agreement between the experimental data and the model prediction.

(b) The 1-D lubrication type model we developed is rather very sensitive to the contact angle measurement. This is because the two competing forces strongly depend on the base radius which also depends on the apparent contact angle. For now the contact angle was predicted using the Cassie-Baxter relation for composite surfaces. This relation is valid for a sessile drop in equilibrium. However, we are investigating an evaporating droplet whose three phase contact line is receding. Hence, a better prediction of the apparent contact angle is necessary to match the experimental data with the model prediction.

(c) This thesis considered only sparse pillars ($\phi_s < 0.15$). We recommend extending the work to include dense pillars (high solid fraction) to gain full understanding of the phenomenon.

(d) The resistance of the gold temperature sensors was drifting and as a result the temperature readings were erroneous. The reason for the drifting is yet unknown. However, we recommend fabricating the temperature sensors from platinum to avoid the resistance drifting problem.

(e) The effect of pillar diameter, height and center-to-center spacing needs to be investigated in a systematic manner to decouple the effect of one from another.

7. Appendix

7.1 Fabrication Process

The steps used to manufacture the test samples are tabulated below. All test samples were manufactured at the Microsystem Technology Laboratory (MTL) at MIT.
Starting substrate: a 150 mm diameter, 600 - 650 μm thick silicon wafer.

Table 7.2: Microfabrication process flow.

process step	process description
RCA clean	clean wafer
oxide growth	thermally grow 200 nm oxide layer
photolithography (front)	HMDS oven spin coat resist prebake oven UV expose develop postbake oven
RIE	remove oxide layer
DRIE	etch silicon
piranha	remove photoresist
RIE	remove oxide layer
photolithography (back)	HMDS oven spin coat resist prebake oven UV expose postbake oven flood expose develop
ebeam	deposit 20 nm chromium deposit 200 nm gold
lift-off	acetone lift-off
packaging	dice wafer using diesaw

7.2 Matlab Script

The following MATLAB code is provided to show the calculations made in computing the forces and the surface superheat.

```
format long;clear all;close all;clc
% Therodynamic properties at 100 °C
rho_liq = 958.35;       % density of liquid water at 100 °C
rho_vap = .59817;       % density of vapor in kg/m.s at T = 100 °C
mu_vap = 1.2269e-5;     % viscosity of vapor in kg/m.s at T = 100 °C
k_vap = 0.02510;        % thermal conductivity of vapor at T = 100 °C
sigma = 0.06358;        % surface tension (N/m) of water at 100 °C
h_fg = 2.2564e6;        % h_fg at T = 99.61 C, P = 1e5 N/m^2
k_sub = 105;            % thermal conductivity of Si at 100 °C

D = 5.2e-6; L = 28.0e-6; H = 22.2e-6;    % pillar array geometry
A = xlsread('C:\Users\sadera\...');
CA_measured = 147 * pi/180;
sf = pi*D^2/(4*L^2);                     % solid fraction
e = 1 - sf;                              % porosity
k_eff = e*k_vap + sf*k_sub;              % effective thermal conductivity
K = (L^2/(4*pi))*(-0.5*log(sf) - 0.738 + sf - 0.887*(sf)^2 + 2.038*(sf)^3);        % permeability
betta = (e/K)^(1/2);
CA_young = 38;                           % Young CA in deg.
P_amb= 101325;
P_cap = 4*cos(CA_young*pi/180)*(sigma/D)/((4/pi)*(L/D)^2-1);
V0 = 0e-9;                               % droplet volume
% based on CB relation
CA_app_CB = acos(-1+sf*(1+cos(CA_young*pi/180)));          % ACA in rad from CB
ACA_CB = CA_app_CB*180/pi;                                 % ACA in deg. from CB
for i=1:1:200
   V(i) = V0+ 0.2*(i-1)*1e-9;
   R0(i) = (3*V(i)./(4*pi)).^(1/3);
   R1(i) = R0(i)*sin(CA_app_CB);
   N(i) = pi*R1(i).^2/L^2;
   F_wet(i) = N(i)*pi*D*sigma*cos(CA_young*pi/180) + rho_liq*V(i)*9.81;
   F_non_wet_by_DT_p(i) = -(pi*e*mu_vap*k_eff/(8*K*H^2*rho_vap*h_fg))*(-
1+2*tanh(.5*H*betta)/(H*betta))^-1*R1(i)^4;
   DT_p(i) = F_wet(i)/F_non_wet_by_DT_p(i);          % superheat based on pillar base temperature
   DT_sub(i) = DT_p(i)*k_eff*620e-6/(H*k_sub);       % temperature drop in the silicon wafer
   DT_tot_a(i) = DT_p(i)+DT_sub(i);                  % total temperature drop
end
% based on measured contact angle
for j=1:1:200
   V(j) = V0+ 0.2*(j-1)*1e-9;
   R0(j) = (3*V(j)./(4*pi)).^(1/3);
   R1(j) = R0(j)*sin(CA_measured);
   N(j) = pi*R1(j).^2/L^2;
   F_wet(j) = N(j)*pi*D*sigma*cos(CA_young*pi/180)+ rho_liq*V(j)*9.81;
   F_non_wet_by_DT_p(j) = -(pi*e*mu_vap*k_eff/(8*K*H^2*rho_vap*h_fg))*(-
1+2*tanh(.5*H*betta)/(H*betta))^-1*R1(j)^4;
   DT_p(j) = F_wet(j)/F_non_wet_by_DT_p(j);          % superheat based on pillar base temperature
   DT_sub(j) = DT_p(j)*k_eff*600e-6/(H*k_sub);       % temperature drop in the silicon wafer
   DT_tot_b(j) = DT_p(j)+DT_sub(j);                  % total temperature drop
end
```

```
plot(A(:,1),A(:,2),'rs',V*1e9,DT_tot_a,'k',V*1e9,DT_tot_b,'b--');
axis([0 20 0 70]);
% error bars
hold on;
errTEMP1 = 0.02*(A(:,2)+100);
errVOL1 = A(:,3);
errorbar(A(:,1),A(:,2),errTEMP1,'rs');
herrorbar(A(:,1),A(:,2),errVOL1,'rs');
set(gca, 'FontWeight', 'BOLD');
xlabel('V (\muL)', 'FontSize', 15,'FontWeight', 'BOLD');
ylabel('superheat, \DeltaT (\circC)', 'FontSize', 15,'FontWeight', 'BOLD');
```

8. Bibliography

[1] C. C. Lee and D. H. Chien, "Thermal and package design of high power laser diodes," 1993, pp. 75-80.

[2] R. Boyd, "Subcooled flow boiling critical heat flux (CHF) and its application to fusion energy components. Part I. A review of fundamentals of CHF and related data base," *Fusion Technol.;(United States),* vol. 7, 1985.

[3] C. Rogers, *et al.*, "Performance of a liquid-nitrogen-cooled, thin silicon crystal monochromator on a high-power, focused wiggler synchrotron beam," *Review of scientific instruments,* vol. 66, pp. 3494-3499, 1995.

[4] I. Mudawar, "Assessment of high-heat-flux thermal management schemes," *Components and Packaging Technologies, IEEE Transactions on,* vol. 24, pp. 122-141, 2001.

[5] S. G. Kandlikar and A. V. Bapat, "Evaluation of jet impingement, spray and microchannel chip cooling options for high heat flux removal," *Heat Transfer Engineering,* vol. 28, pp. 911-923, 2007.

[6] I. Pioro, *et al.*, "Nucleate pool-boiling heat transfer. I: review of parametric effects of boiling surface," *International Journal of heat and mass transfer,* vol. 47, pp. 5033-5044, 2004.

[7] J. R. Thome, "Boiling in microchannels: a review of experiment and theory," *International Journal of Heat and Fluid Flow,* vol. 25, pp. 128-139, 2004.

[8] R. A. Taylor and P. E. Phelan, "Pool boiling of nanofluids: comprehensive review of existing data and limited new data," *International Journal of heat and mass transfer,* vol. 52, pp. 5339-5347, 2009.

[9] S. Kim, *et al.*, "Surface wettability change during pool boiling of nanofluids and its effect on critical heat flux," *International Journal of heat and mass transfer,* vol. 50, pp. 4105-4116, 2007.

[10] F. P. Incropera, *et al.*, *Fundamentals of heat and mass transfer*: Wiley, 2011.

[11] S. You, *et al.*, "Effect of nanoparticles on critical heat flux of water in pool boiling heat transfer," *Applied Physics Letters,* vol. 83, p. 3374, 2003.

[12] K. H. Chu, *et al.*, "Structured surfaces for enhanced pool boiling heat transfer," *Applied Physics Letters,* vol. 100, p. 241603, 2012.

[13] R. Chen, *et al.*, "Nanowires for enhanced boiling heat transfer," *Nano letters,* vol. 9, pp. 548-553, 2009.

[14] E. N. Wang, *et al.*, "Micromachined jets for liquid impingement cooling of VLSI chips," *Microelectromechanical Systems, Journal of,* vol. 13, pp. 833-842, 2004.

[15] L. Lin and R. Ponnappan, "Heat transfer characteristics of spray cooling in a closed loop," *International Journal of heat and mass transfer,* vol. 46, pp. 3737-3746, 2003.

[16] J. Kim, *et al.*, "Evaporative spray cooling of plain and microporous coated surfaces," *International Journal of heat and mass transfer,* vol. 47, pp. 3307-3315, 2004.

[17] A. Jiao, *et al.*, "Thin film evaporation effect on heat transport capability in a grooved heat pipe," *Microfluidics and Nanofluidics,* vol. 1, pp. 227-233, 2005.

[18] H. Wang, *et al.*, "Characteristics of an evaporating thin film in a microchannel," *International Journal of heat and mass transfer,* vol. 50, pp. 3933-3942, 2007.

[19] H. Wang, *et al.*, "An analytical solution for the total heat transfer in the thin-film region of an evaporating meniscus," *International Journal of heat and mass transfer,* vol. 51, pp. 6317-6322, 2008.

[20] H. Ma and G. Peterson, "Temperature variation and heat transfer in triangular grooves with an evaporating film," 1996.

[21] R. Xiao, *et al.*, "Multilayer liquid spreading on superhydrophilic nanostructured surfaces," *Applied Physics Letters,* vol. 94, p. 193104, 2009.

[22] R. Xiao, *et al.*, "Prediction and optimization of liquid propagation in micropillar arrays," *Langmuir,* 2010.

[23] K. H. Chu, *et al.*, "Uni-directional liquid spreading on asymmetric nanostructured surfaces," *Nature materials,* vol. 9, pp. 413-417, 2010.
[24] J. Bico, *et al.*, "Wetting of textured surfaces," *Colloids and Surfaces A: Physicochemical and Engineering Aspects,* vol. 206, pp. 41-46, 2002.
[25] L. Zheng, *et al.*, "Superhydrophobicity from microstructured surface," *Chinese Science Bulletin,* vol. 49, pp. 1779-1787, 2004.
[26] F. J. Norton, "Waterproofing treatment of materials," ed: U.S. Patent No. 2,386,259., 1945.
[27] L. Gao and T. J. McCarthy, "A Commercially Available Perfectly Hydrophobic Material (θA/θR= 180°/180°)," *Langmuir,* vol. 23, pp. 9125-9127, 2007.
[28] T. Onda, *et al.*, "Super-water-repellent fractal surfaces," *Langmuir,* vol. 12, pp. 2125-2127, 1996.
[29] S. Shibuichi, *et al.*, "Super water-repellent surfaces resulting from fractal structure," *The Journal of Physical Chemistry,* vol. 100, pp. 19512-19517, 1996.
[30] D. Quéré, "Wetting and roughness," *Annu. Rev. Mater. Res.,* vol. 38, pp. 71-99, 2008.
[31] R. N. Wenzel, "Resistance of solid surfaces to wetting by water," *Industrial & Engineering Chemistry,* vol. 28, pp. 988-994, 1936.
[32] A. Cassie and S. Baxter, "Wettability of porous surfaces," *Trans. Faraday Soc.,* vol. 40, pp. 546-551, 1944.
[33] N. A. Patankar, "Transition between superhydrophobic states on rough surfaces," *Langmuir,* vol. 20, pp. 7097-7102, 2004.
[34] M. Callies and D. Quéré, "On water repellency," *Soft matter,* vol. 1, pp. 55-61, 2005.
[35] D. Quéré, *et al.*, "Slippy and sticky microtextured solids," *Nanotechnology,* vol. 14, p. 1109, 2003.
[36] M. Reyssat, *et al.*, "Impalement of fakir drops," *EPL (Europhysics Letters),* vol. 81, p. 26006, 2008.
[37] E. Bormashenko, *et al.*, "Cassie-wenzel wetting transition in vibrating drops deposited on rough surfaces: Is the dynamic cassie-wenzel wetting transition a 2D or 1D affair?," *Langmuir,* vol. 23, pp. 6501-6503, 2007.
[38] E. Bormashenko, *et al.*, "Resonance Cassie-Wenzel wetting transition for horizontally vibrated drops deposited on a rough surface," *Langmuir,* vol. 23, pp. 12217-12221, 2007.
[39] Z. Han, *et al.*, "Electrowetting control of cassie-to-wenzel transitions in superhydrophobic carbon nanotube-based nanocomposites," *ACS nano,* vol. 3, pp. 3031-3036, 2009.
[40] T. N. Krupenkin, *et al.*, "Reversible wetting-dewetting transitions on electrically tunable superhydrophobic nanostructured surfaces," *Langmuir,* vol. 23, pp. 9128-9133, 2007.
[41] P. Tsai, *et al.*, "Evaporation-triggered wetting transition for water droplets upon hydrophobic microstructures," *Physical review letters,* vol. 104, p. 116102, 2010.
[42] T. Zhang, *et al.*, "High-Temperature Wetting Transition on Micro-and Nanostructured Surfaces," *Angewandte Chemie International Edition,* vol. 50, pp. 5311-5314, 2011.
[43] K. Smyth, *et al.*, "Dynamic wetting on superhydrophobic surfaces: Droplet impact and wetting hysteresis," 2010, pp. 1-8.
[44] H. M. Kwon, *et al.*, "Rapid Deceleration-Driven Wetting Transition during Pendant Drop Deposition on Superhydrophobic Surfaces," 2011.
[45] T. Deng, *et al.*, "Nonwetting of impinging droplets on textured surfaces," *Applied Physics Letters,* vol. 94, p. 133109, 2009.
[46] B. Gottfried, *et al.*, "The Leidenfrost phenomenon: film boiling of liquid droplets on a flat plate," *International Journal of heat and mass transfer,* vol. 9, pp. 1167-1188, 1966.
[47] H. Kim, *et al.*, "On the effect of surface roughness height, wettability, and nanoporosity on Leidenfrost phenomena," *Applied Physics Letters,* vol. 98, p. 083121, 2011.
[48] D. A. Nield and A. Bejan, *Convection in porous media*: Springer Verlag, 2006.
[49] J. Bico, *et al.*, "Pearl drops," *EPL (Europhysics Letters),* vol. 47, p. 220, 1999.
[50] G. Peterson, "An Introduction to Heat Pipes: Modeling, Testing and Applications,(1994)," ed: Wiley, New York.

[51] A. Sangani and A. Acrivos, "Slow flow past periodic arrays of cylinders with application to heat transfer," *International journal of Multiphase flow,* vol. 8, pp. 193-206, 1982.